PARTICLE TRACKING VELOCIMETRY APPLIED TO AN OPPOSED-JET MIXER CONFIGURATION

A Thesis

Presented in Partial Fulfillment of the Requirements for

The Degree Master of Science if the

Graduate School of The Ohio State University

By

Dong Zhang, B.S.

*****

The Ohio State University
2002

Master's Examination Committee

Dr. Robert S. Brodkey, Adviser

Dr. Shang-Tian Yang

Approved by

Department of Chemical Engineering

ABSTRACT

Mixing vessels are widely used for blending and chemical reactions. Although much has been done on mixing processes, the complex, three-dimensional flow phenomena are still not well understood. The purpose of the first step in this research is to obtain the experimental data for validation of simulation and validation of time-resolved, three-dimensional velocity vector data. Such results are an essential part of the design of mixing systems. Our current mixing investigations have been carried out experimentally in order to examine the turbulent flow of the opposed jet reactor. The inlets are laminar at Reynolds number of 2,000. A particle tracking velocimeter (PTV) was utilized in this research. The spatial resolution was improved over our previous system by four (684x484 pixels) and at the same time the time resolution was improved to 60 Hz (although in this work the temporal resolution was 30 Hz). By using two synchronized video cameras (master and slave), two PC computers could be used to analyze the experimental velocity vector data and discover the mixing characteristics of the opposed jet reactor.

After obtaining the stereoscopically flow field images, the minimum number (11) of average frames was determined and the two-dimensional, dynamic movies of three views (front, top, and side) could then be used to describe the dynamic characteristics. In

addition to the dynamic movies, the long time (36,000 averaged images) and the instantaneous characteristics will be addressed. The final part of the analysis of the experimental data is to determine an initial condition for the subsequent computational efforts. This initial condition needs to satisfy continuity by determination of the $\partial U_x/\partial x$ term from the continuity equation. The term can also be established by using Taylor's hypothesis. Thus the continuity equation evaluation and using Taylor's hypothesis will be compared.

Dedicated to my parents

ACKNOWLEDGMENTS

I would like to acknowledge the efforts of some of the many people who helped me in the course of my graduate studies. First and foremost I would like to thank Dr. R. S. Brodkey with deepest gratitude for his guidance, suggestion, encouragement, and financial support through the whole period of my M.A. research. Thank you for helping me to become a more independent researcher and a more confident person. I also thank Dr. Jeffery Chalmers being a member of my examination committee. Thank you so much Dr. Brodkey and the faculty and staff of ChemE.

I thank Dr. Yang Zhao, for the stimulating discussions which led to many of the ideas and helping me get all the things I need in this research. From the optics to analysis you were there for me. Thank you for your lessons and your friendship. I most certainly do not want to forget the good partner of my group, Matthew Nilsen. Thank you very much!

VITA

October 29, 1977	Born – Tianjin, China
September, 2000	B.S. Engineering (ChE.), Tianjin University, Tianjin, China
2000-Present	Graduate School, Chemical Engineering Department, The Ohio State University, Columbus, Ohio

FIELDS OF STUDY

Major Field: Chemical Engineering
Minor Field: Image Processing and Analysis, and Fluid Mechanics

TABLE OF CONTENTS

Page

Abstract....................ii

Dedication....................iii

Acknowledgments....................v

Vita....................vi

List of Tables....................xii

List of Figures....................xiii

Chapters:

1. Introduction....................1
    - 1.1 Research Introduction....................1
    - 1.2 Previous Studies of Velocity Vector Measurement Techniques on the Opposed Jet mixer....................2
    - 1.3 Observational Background of the Opposed Jet Reactor....................5
    - 1.4 Computational Fluid Dynamics (CFD)....................6
    - 1.5 Research Objective....................7
2. Literature review....................9
    - 2.1 Overview of Mixing Concepts....................9
    - 2.2 Previous Research of Opposed Jets....................10

2.3 Velocity Vector Measurement Techniques..............................21

- 2.3.1 Particle Image Velocimetry......................................22
- 2.3.2 Particle Tracking Velocimetry...............................23
- 2.3.3 Hot Wire Anemometers...25
- 2.3.4 Laser Doppler Aanemometry..................................27

2.4 Visualization Technique Determination....................................28

3. Research Process Description and Experiment Equipment....................30

3.1 Impinging Flow System Setup and Operation Procedure.............31

- 3.1.1 Schematic of the Opposed Jet Geometry..............................34

3.2 Optical Setup and Operational Procedure...................................35

- 3.2.1 Illumination Source..36
- 3.2.2 Indoor Preparation...38

3.3 Experimental Hardware and Software......................................38

- 3.3.1 Processing Hardware..39
  - 3.2.3.1 CCD Cameras..39
  - 3.2.3.2 Optics Recording Equipment.................................41
  - 3.2.3.3 The Tracking Particles...42
- 3.3.2 Processing Software...43

3.4 Experimental Procedure and Apparatus Setup............................44

- 3.4.1 Threshold Preparation..44

3.4.2 Steps Undertaken in Experiment....................................45

3.4.3 Detailed Software Analysis Procedure..............................48

3.4.4 Grabbing Images Software Digitization Procedure.................49

3.4.5 Determine Threshold and Particle Distance Parameters...........50

3.4.6 Image Pre-processing..51

3.4.7 Image Background Subtraction.....................................52

3.4.8 Determination of 2-D Particle Positions.............................53

3.4.9 Image Analysis Program 2-D Tracking..............................53

3.4.10 Image Analysis Program 3-D Matching.............................54

3.4.11 Adaptive Gaussian Window (AGW) Validation...................55

3.4.12 Average Image..56

3.4.13 Matlab Conversion..56

3.4.14 Image File Types Conversion.......................................56

4. Statistical Calculation and Comparison of the Velocity Vector Data...........57

4.1 Computation by the Continuity Equation and Taylor's Hypothesis Methods...57

4.2 Numerical Differentiation of Equally Spaced Experimental Data......60

4.3 Least Squares Power Functions..61

4.4 Smoothing..61

4.5 Selection of Number of Points and Degree of Fit in Each Strip.........62

4.6 Numerical Differentiation of Equally Spaced Data........................62
  4.6.1 Smoothing Formulas..62
  4.6.2 Sloping Formulas..63
4.7 Computation Code by Using the Continuity and Taylor's Method..64
4.8 Statistical Analysis Between the Continuity Equation and Taylor's Hypothesis Using $U_{\text{local velocity}}$ and $U_{\text{overal velocity}}$..............................66
  4.8.1 Comparision Between Continuity and Taylor's Hypthesis Using $U_{\text{localvelocity}}$..67
  4.8.2 Comparision Between Continuity and Taylor's Hypthesis Using $U_{\text{overal velocity}}$..69
5. Results and Discussion...72
5.1 Statistical Analysis of the Fluid Field 73
5.2 Determination of Average Number to Obtain a Reasonable Statistical Average 80
5.3 Graphical Analysis for the Average Fluid Field and Instantaneous Fluid Field 82
  5.3.1 Graphical Analysis for the Average Fluid Field.......................82
  5.3.2 Graphical Analysis for the Instantaneous Fluid Field.................87
6. Conclusion and Recommendations..90

6.1 Conclusions..90

6.2 Recommendations..91

6.2.1 Camera Spatial Resolution Recommendation.........................91

6.2.2 Cameras Arrange Recommendation...................................92

6.2.3 Particle Path Investigations Recommendation.........................93

Bibliography...94

Appendix: Experimental Equipments and Computer Codes.................................98

LIST OF TABLES

Table Page

1 Comparison of flow visualization techniques....................................28

2 Total vector number in each data set..49

3 Descriptive statistics of two $\partial U_x/\partial x$ results at $U_{\text{local velocity}}$ condition............69

4 F-Test: Two-Sample for variances at $U_{\text{local velocity}}$ condition......................70

5 T-Test: Two-Sample assuming unequal variances at $U_{\text{local velocity}}$ condition....70

6 Descriptive statistics of two $\partial U_x/\partial x$ results at $U_{\text{overal velocity}}$ condition...........71

7 F-Test: Two-Sample for variances at $U_{\text{overal velocity}}$ condition.....................72

8 T-Test: Two-Sample assuming unequal variances at $U_{\text{overal velocity}}$ condition...72

9 Total vector number in each data set...74

10 X-direction velocity values in each data set..75

11 Y-direction velocity values in each data set..76

12 Z-direction velocity values in each data set..77

13 Velocity values in each data set..78

14 Vector # needed in each velocity direction at different statistical factors.......81

15 Orthogonal Least Squares coefficients for third-degree smoothing formulas...105

16 Orthogonal least squares coefficients for sloping formulas.......................105

LIST OF FIGURES

Figure Page

1 Impingement mixing of two streams of glycerine water mixtures in a 3.2 mm diameter Plexiglass chamber Re = 90 12

2 (a) Lamellar structure formed by stretching flow during impingement (b) Local lamellar structure showing the definitions of striation thickness and coordinate system on interface 14

3 Long time 9-1/2 min, average at a jet Reynolds number of 200 on a 21^3 grid 17

4 Three-dimensional, time-averaged velocity vectors in the horizontal (xy) plane with contours and surface map of z-vorticity at a Reynolds number of 4,000 19

5 Three-dimensional, time-averaged velocity vectors in the horizontal (xy) plane with contours and surface map of z-vorticity at a Reynolds number of 200 20

6 Opposed jet flow system 32

7 Schematic diagram of the impinging jet system 33

8 Photograph of the impinging jet system 34

9 Front view of system with flash lighting and cameras 35

10 Front view of recording equipment and analysis equipment 40

11 Front view of recording equipment and analysis equipment........................40

12 Flow chart for experiment process..44

13 Flow chart for code process..47

14 Taylor's hypothesis theory..60

15 Matlab^{TM} program flow chart..67

16 X, Y, Z direction mean vs. vector numbers..79

17 X, Y, Z direction standard deviation vs. vector numbers............................79

18 X, Y, Z direction skewness vs. vector numbers......................................80

19 X, Y, Z direction kurtosis vs. vector numbers.......................................80

20 3-D, time-averaged, velocity vectors in the horizontal (xy) plane (a), the jet (yz) plane (b), and the lateral (xz) plane (c)..84

21 Long-time averaged velocity field at a jet Reynolds number of 2,000................86

22 Long-time, average 3-D velocity fields of front (a) and top views (b) at a jet Reynolds number of 2,000...87

23 11-frame average results of the front view flow for 11-frame averages at a jet Reynolds number of 2,000...89

24 11-frame average results of the top flow for 11-frame averages at a jet Reynolds number of 2,000...90

25 Recommendation configuration of the three-camera system........................94

CHAPTER 1

INTRODUCTION

1.1 Research Introduction

Mixing basically means blending one mass into another. It is "a complex of two or more ingredients which do not bear a fixed proportion to one another and which, however thoroughly commingled, are conceived as retaining a separate existence" [1].

Mixing is widely used in chemical reactions. It is “an essential and ubiquitous component in mining, food, petroleum, chemicals, pharmaceuticals, pulp and paper, and power industries, and in municipal and industrial waste treatment, to name a few” [2]. From simple reactions to complex multi-phase reactions, mixing can affect the reaction rate, yield, and selectivity. Ineffective mixing in these reaction systems may have a large negative effect on production and selectivity [3]. The waste product can be increased, which may increase environmental impacts and operational cost. Thus it is very important to ensure effective mixing in such processes.

Our current mixing research mainly focuses on the opposed jet mixer, which is important for solid thermal drying, engine combustion, and pharmaceutical crystallization. The two jets discharging into the confined region are often found in engineering applications involving the mixing of two streams of fluid for the purposes of chemical reaction, combustion, heat transfer, and gas-solid impingement. The opposed jet mixer has several advantages and can be utilized in place of stirred tanks. By using the small-scale opposed jet mixer, mixing will be investigated experimentally using quantitative particle-tracking velocimetry. The objective is to achieve useful design information and minimize negative product yield.

1.2 Previous Studies of Velocity Vector Measurement Techniques on the Opposed Jet Mixer

The previous studies of velocity vector measurement techniques chosen for the opposed jet mixer investigations include hot wire anemometry (HWA), laser doppler anemometry (LDA), particle image velocimetry (PIV), and particle tracking velocimetry (PTV).

Hot wire anemometers are sensors used for measuring velocity. Thermal anemometers measure fluid velocity by sensing changes in heat transfer from a small, electrically heated sensor exposed to the flow. Hot wire anemometry is able to provide some useful supplementary information on the turbulence characteristics due to the availability of long time sequences of data.

Particle image velocimetry, which can measure two components of velocity easily in a 2-D plane based on photographic imaging, has become the state-of-the-art experimental technique for fluid velocity measurement. Flow visualization with PIV involves seeding the fluid with particles, which are assumed to follow the flow path lines, and then measuring their velocity by correlation techniques in two sequential pictures. It employs "laser light sheets and planar imaging media (e.g., photographic film or video CCD cameras) to measure the two in-plane components of fluid velocities in a planar domain in a flow or three components in a planar domain if a stereoscopic imaging technique is used" [4].

Particle tracking velocimetry provides "the lagrangian representation of the flow field; every seeding particle is traced along its trajectory within the illuminated volume" [5]. Most PTV techniques use streak photography as a tool to determine the flow field. The velocity field can be obtained by measuring length, orientation, and location of each streak.

Haam et al. [6] and Haam and Brodkey [7] studied the opposed jet mixer by using particle tracking velocimetry. Their ultimate goal is to have a full numerical simulation to reproduce the experimental flow field and make future experiments unnecessary. There are two aspects to their research: one is the experimental velocity measurement and the other is the computational simulation of the same information data. The overall project goal is to provide comparisons of the experimental data and the simulated results from the computational approach. This research is considered the first step toward the development of new technology for fast mixing of chaotic flow.

In 1998, Zhao et al. [3] also measured the velocities over a range of jet Reynolds numbers from 200-5000 by PTV. For higher jet Reynolds numbers (> 200), the jets are not stable. Due to the jet motion of flapping or jet oscillation, long-time ensenmbled averages are necessary. By examining a sequence of frames, the laminar flow inlet velocity does appear to have large-scale motions of the jets in the flow field.

Computational fluid dynamics (CFD) is the science of predicting fluid flow, heat transfer, mass transfer, chemical reactions, and related phenomena by solving the mathematical equations that governs these processes using a numerical algorithm. The results of CFD are relevant engineering data used in conceptual studies of new designs, detailed product development, troubleshooting, and redesign. Computational fluid dynamics is now widely used to predict flow fields in industrial mixers owing to its short turnover time and low cost. With the application of CFD simulation at the time-average level, the process variables such as mean velocity distribution, time scales, distribution of kinetic energy, and dissipation rate can be obtained. The practical modes of CFD are based on solving the Reynolds averaged Navier-Stokes equations (RANS) with the flow model. The key work of our research is to "test whether the direct numerical simulation (DNS) calculation can simulate the experimental flow field, then by means of such a calculation, the Navier-Stokes equations' individual terms can be measured" [8].

Direct numerical simulation (DNS) is the method in which all of the scales of motion of a turbulent flow are computed down to the grid size used in the computation. DNS is the most exact approach for turbulence simulation to solve the Navier-Stokes equations without averaging or approximation. The result is a single realization one instant in time of a flow and is equivalent to a short duration laboratory experiment. DNS can be only carried out at relatively low Reynolds numbers. For homogeneous turbulent flows, the Reynolds number of interest must be based on the turbulent velocity and length scales. The ability to compute flows with turbulent Reynolds numbers of 100 actually allows DNS to reach the low end of the range of Reynolds numbers of engineering interests [9]. Whenever DNS is feasible for a given flow, it should be the method of choice, especially when a study of the detailed physics of the flow is the goal.

Large eddy simulation (LES) is "an approach in which the largest scales of motion are represented explicitly while the small scales are treated by some approximate parameterization or model" [10]. LES is three-dimensional and time-dependent and thus expensive, but should be much less costly than a DNS of the same flow. As a result, LES has come to occupy a kind of middle ground. Use of LES is a good choice for investigating flows that are too complex to be computed economically by DNS; in practice, with today's computers, this means any flow, which is inhomogeneous in more than one direction. LES is now becoming powerful enough to be worthy of consideration as a method to be employed selectively [10].

1.3 Observational Background of the Opposed Jet Reactor

A study of the mixing process includes several basic considerations. The first is the effect of the vessel on the mixing process. Vessel geometry, dimensions, and structure may dictate mixer selection and mixing performance, because some mixing processes are best accomplished in vessels of specified size and shape. Often, existing in-plant vessels are poor choices for a specified mixing result.

There are several reasons for the selection of the opposed jet geometry. Two of these are associated with an undressed problem with DNS calculations in the past on channel, pipe, and boundary conditions at the entry to the flow. In the standard approach, the inlet turbulent conditions are unknown, thus one assumes that the inlet conditions are the same as that obtained from the computation at the exit. This is called cyclic boundary conditions. In contrast, the opposed jet system operates with laminar flow inlets, even for conditions where the jets are unstable. In our opposed jet mixer, cyclic boundary conditions are not needed [11].

The second reason is the mixing method. The standard method of achieving effective mixing is through the use of the opposed jet mixer. There are many kinds of jets applied in the mixing process, including planar jets, free jets, and axisymmetric jets in specific geometries; however, not too many people focus on the industry-used opposed jets mixer in the cylindrical reaction chamber. The opposed jets mixer can be utilized on many aspects of the industry process, such as reaction injection molding, automobile combustion, and chemical reactors.

1.4 Computational Fluid Dynamics (CFD)

The first step in CFD is to use the direct numerical simulation (DNS) approach to analyze the opposed jet mixer model. DNS uses "numerical simulation of the unsteady 3-dimensional Navier-Stokes equations with appropriate boundary conditions to resolve the evolution of all dynamically significant scales of motion" [12]. Important issues here are that cyclic boundary conditions are not needed, because the opposed jet system operates with laminar flow inlets, even for conditions where the jets are unstable. We do not expect to be able to match results on an instantaneous basis, but by tracking important long-time average, we can evaluate this approach for engineering purposes. After the experimental results are available, the results need to be compared with the direct numerical simulation and then extended to higher Reynolds numbers using the large eddy simulation efforts.

This whole research is a multistep process including unsteady flows calculated by DNS, the simulation solved by LES, the extension of LES to higher Reynolds numbers, and finally the Reynolds averaged Navier-Stokes (RANS) that can be extensively used in industry.

1.5 Research Objective

Our current mixing investigations have been carried out experimentally in order to examine the turbulent flow (Re = 2,000) of the opposed jet reactor. A new particle tracking velocimetery was utilized in this research. The spatial resolution was improved by four (684x484 pixels) and at the same time the time resolution could be improved by two (although in this work the temporal resolution was 30 Hz). By using two synchronized video cameras, the two PC computers could be used to analyze the experimental velocity vector data and the mixing characteristics of the opposed jet reactor. After obtaining the stereoscopically flow field images, the minimum number (11) of frames in a moving window average was determined. From these frames, the dynamic movies of three views (front view, top view, and side view) were used to describe the opposed jet mixing characteristic. The long time (36,000 averaged images) as well as the instantaneous characteristics will be addressed in their work.

After obtaining the stereoscopically flow field images, the minimum number (11) of average frames was determined and the two-dimensional, dynamic movies of three views (front, top, and side) could then be used to describe the dynamic characteristic. In addition to the dynamic movies, the long time (36,000 averaged images) and the instantaneous characteristics will be addressed.

The final part of the analysis of the experimental data is to determine an initial condition for the subsequent computational efforts. This initial condition needs to satisfy continuity by determination of the $\partial U_x/\partial x$ term from the continuity equation. The $\partial U_x/\partial x$ term to be determined by the continuity equation. The term can also be established by using Taylor's hypothesis. Thus the continuity equation evaluation and using Taylor's hypothesis will be compared.

CHAPTER 2

LITERATURE REVIEW

The objective of this study is to determine the mixing characteristics of the opposed jet reactor. Chapter 2 will provide the previous basic ideas about the mixing concepts and visualization techniques that have been utilized in earlier research to obtain the opposed jet reactor flow field.

2.1 Overview of Mixing Concepts

Mixing is, in the strict sense, "a transient process from initial segregation to ultimate homogeneity" [13]. The basic concept of mixing is "putting together two or more initially segregated constituents and stirring, in order to attain uniformity, a new product, or the complete disappearance of one of the constituents, etc" [14].

The nature of stirring divides into two classes, depending on whether the Reynolds number of the flow is large or small. The Reynolds number is defined as the ratio of inertial forces to viscous forces in the flow, $Re = UL/\nu$, where U is the velocity scale, L is the length scale in the flow, and ν is viscosity [15].

Typically, in the inlet tubes, when Re > 2,000, which are our current opposed jet flow conditions, the flow remains laminar in the inlet. In our opposed jet mixer, the jets impinge and recirculation regions form above and below the impingement point.

At low Reynolds number, typically at Re < 10, friction is large, and thus the cost of stirring is high. The jets do not impinge and the velocity field scales linearly with the Reynolds number. The flow stops immediately and the mechanical agitation is switched off. In this condition, mixing can be very inefficient.

2.2 Previous Research of Opposed Jets

A previous study of the opposed jet systems has dealt with the reaction injection molding (RIM). Lee et al. [16] focused on the impingement mixing of fast polymerizing reactants, which is a unique aspect of the RIM process. Reaction injection molding was examined in terms of a simplified model, which includes both fluid mechanical and polymerization aspects of the problem. Within a specific geometry, the preliminary impingement mixing model, the combination of local stretching flow, and fast, laminar polymerization have the virtue of simplicity and seem to give the correct magnitude for striation thickness and correct trends with mixer head geometry, and Reynolds number dependence. The flow structures were imaged as a function of the inlet Reynolds numbers and the feedback could provide useful information to enhance the mixing in impinging jets.

At the same time, Tucker and Suh [17] conducted similar research on RIM. Flow visualization experiments were used to find the point of transition to turbulent mixing flow. This transition occurred at a nozzle Reynolds number of 140 for directly opposed nozzles and at higher Reynolds numbers for nozzles angled downstream.

Kolodziej et al. [18] used the optical microscopy on the resultant polymer from RIM to measure the striation thickness distribution. They found that the average thickness decreased with increasing Rej. Without reporting the observed flow patterns or flow field in the mixer, Ogawa and Maki [19] carried out steady state calculations of low Reynolds number flows. Wood et al. [20] presented a study of the flow field created when two cylindrical laminar jets were impinged head-on near the closed end of a cylindrical mixing chamber. The flow field was investigated by using three-dimensional numerical simulation, particle tracking, and laser doppler anemometry. Their conclusion was that when the Reynolds number was greater than 75, the on-set of oscillations appeared and the flow became unsteady and turbulent because the oscillations moved the jets off-center, so that direct impingement no longer occurred. Johnson et al. [21] discussed the effect of geometrical parameters on the flow field of jet Reynolds numbers from 200 to 500.

In 1980, Lee et al. [22] extended the impingement mixing to the fast polymerizing reactants through the RIM (Reaction Injection Molding) process. RIM is a manufacturing process used to make large plastic parts. RIM offers a number of advantages over other processes for molding large plastic parts, e.g., excellent surface finish, inexpensive processing equipment, etc. In this process, two liquid resins are rapidly metered, mixed, and delivered to a mold where they react and cure to form a solid polymeric part. Lee et al. [23] developed a laboratory scale RIM machine which used positive displacement cylinders for metering and by impingement mixer. They had used this device to perform a number of experiments on impingement mixers. Lee et al. also created a qualitative impingement mixing which involves the creation of a rapid fluid motion that reduces the distance between reactants or striation thickness [24]. This thickness is small enough that molecular diffusion can bring the reactants together in a time scale less than the time scale of polymerization in Fig. 2.1. By this assumption, the RIM model will consider the fluid mechanics of impingement, molecular diffusion. By using the reaction exotherm of the mixture as an indication of the mixing quality, the results showed an exotherm, which increased with Reynolds number up to a maximum value and remained at this level at that value for all higher Reynolds numbers. The Reynolds number at which this plateau was reached increases with increasing reactivity of the resins (i.e., with decreasing time allowed for diffusion).

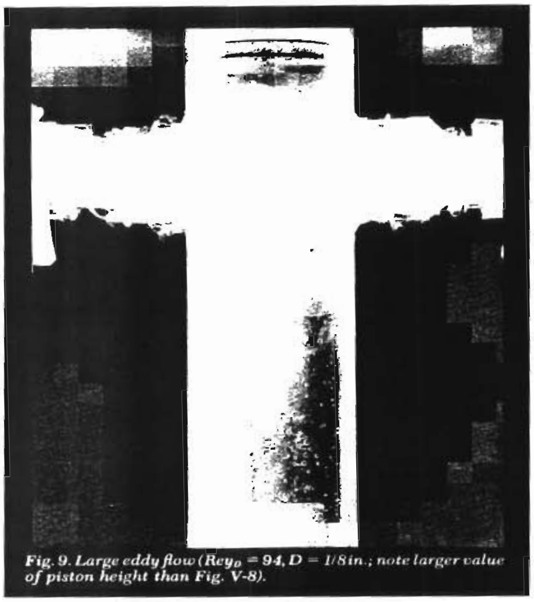

Fig. 2.1 Impingement mixing of two streams of glycerine water mixtures in a 3.2 mm diameter Plexiglass chamber: Re = 90. [22]

The overall picture is consistent with a scale of segregation, which decreases continuously with increasing Reynolds number. For any particular resin system, there is some scale of segregation that is sufficiently small so that complete reaction is achieved. Lee et al. tested both a head-on impingement configuration as well as a configuration in which the nozzles were angled toward the closed end of the mixing chamber and offset from the chamber centerline. These two geometries performed identically at the same Reynolds number range (for the more viscous component) from 40 to 250. For material with a 6 seconds gel time, complete mixing was obtained at a Reynolds number of 250.

After Lee et al. set three different Reynolds numbers, 50, 90, and 150, the flow impingement process was taken by using high-speed photographs. The jets were detached from the wall at Re = 50 and vortex was formed. Detachment is the first step for effective mixing. At the center of this vortex, the fluid layers were less than 100μm apart; however, other parts of the flow were much more poorly mixed. The vortex motion was most intense around the impingement point, dying away downstream. At Re = 150, there were apparently many vortices which were moving so rapidly that they could not be stopped by the flash speed.

As Fig. 2.2 indicates, the flow in an impingement geometry is very chaotic and often can not be modeled in detail. The qualitative impingement mixing involves the creation of a rapid fluid motion, which reduces the distance between reactants or striation thickness. The "s" is "small enough that molecular diffusion can bring them together in a time scale less than the time scale of polymerization" [25].

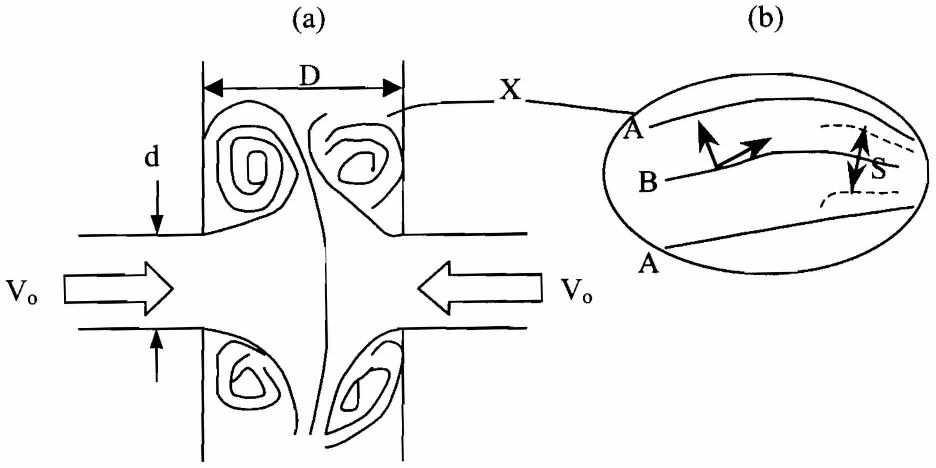

Fig.2.2 (a) Lamellar structure formed by stretching flow during impingement (b) Local lamellar structure showing the definitions of striation thickness and coordinate system on interface. [22]

Moreover, Malguaranera and Suh [26] studied impingement mixing by using glycerin as a model fluid. This work contained the 2-D analysis of impingement mixing. They used a sample variance technique to measure mixing quality and found that the measured mixing quality depended on only two parameters, the Reynolds number and momentum ratio. Their fluid delivery system was pressure driven as opposed to the more common positive displacement type and, for any value of momentum ratio other than unity, the fluid delivery system crossfed. At this condition, the fluid with the higher momentum was forced through the opposite nozzle and back up into the other fluid delivery line. This is probably a characteristic peculiar to the particular delivery system; no mention of this type of behavior with positive displacement pumping schemes has been made in the literature.

An increase in Reynolds number from around 250 (the lowest value tried) to around 500 improved the measured mixing quality. But further increasing in Reynolds number (up to around 3,000) brought no improvements in mixing. At Reynolds numbers of 500 and above, the standard deviation among samples (used to determine mixing quality) was around 2 percent of the mean. This is a reasonable value for the accuracy of the titration technique used in these experiments to measure the concentration in each sample. Therefore, it is possible that the mixing quality measurement technique "bottomed" around the Reynolds number of 500, and failed to detect further improvements in mixing. If this is so, then other conclusions of this work regarding the unimportance of other dimensionless groups are open to question.

In 1998, Zhao and Brodkey [27] furthered their study from RIM type impinging jets to the opposed jet reactor. Instead of using dye injection techniques, they introduced small, neutrally buoyant particles and use tracking techniques. The dyed particles uniformly existed in the flow and were small; they were neutrally bright enough to ensure the particles to follow the flow motion. Thus, the particle motions were assumed to be the local and instantaneous flow motions.

The opposed jet mixer experiments were done by using the particle-tracking technique. Zhao and Brodkey [28] found two steady state flow regions: for Reynolds number < 10, the jets did not impinge and the velocity field scaled linearly with Reynolds number; for Reynolds number > 10, the jets began to impinge and recirculation regions formed above and below the impingement point. There is a good agreement between the computational and experimental flow fields. Equation 2.1 is used to calculate the inlet Reynolds number of the opposed jet mixer.

$$Re = d_j U_o \rho / \mu \qquad (2.1)$$

Where:

d_j = inlet jet diameter

U_o = inlet average jet velocity

ρ = density of the flow liquid

μ = molecular viscosity

Three locations were found with high rates of stretching occurring:

1) Where the jet fluid separated from the jet entrances.
2) At the contactor exit
3) At the impingement point

Later, Zhao and Brodkey concentrated on when the flow is laminar (Re = 200) [11]. The long time average period was about 9 minutes. The average results were calculated by using the PTV measured velocities. In Fig. 2.3, the color stands for the magnitude of the flow speed, red being high and magenta being low. On the average, the flow motion looks regular. But the real flow is not the long-time average. In reality, this opposed jet mixer flow is anything but steady. Even at laminar flow associated with the inlet velocity Re = 200, there are large-scale variations and motions of the jets in the flow field.

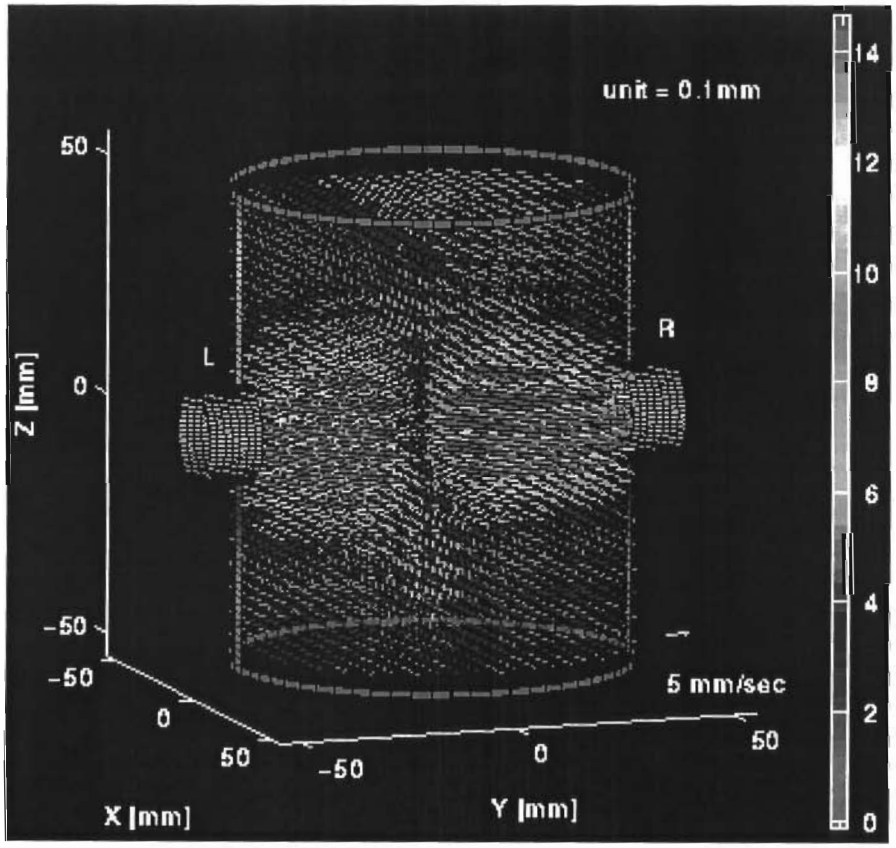

Fig. 2.3 Long time 9-1/2 min, average at a jet Reynolds number of 200 on a 21^3 grid. [27]

Since the flow in such an opposed jet reactor is very complex, the technique following single particle movement or groups of particles movement is also useful to help determine the flow structure and dynamics. By tracking many particles in the flow, Zhao and Brodkey [29] found the full-field, time-averaged flow at Re = 200. The particle paths here described the mixing dynamic and helped us to visualize the flow interactions and obtain a better picture of the mixing dynamic from the time domain point of view.

As shown in Fig. 2.4 about the full, 3-D view of the flow, the inlet flow is a laminar flow of Reynolds number of 4,000 with nearly 1/2 million velocity vectors. The vectors are shown with seven levels of color and are on a 21^3 grid. The flow field is very random and complex.

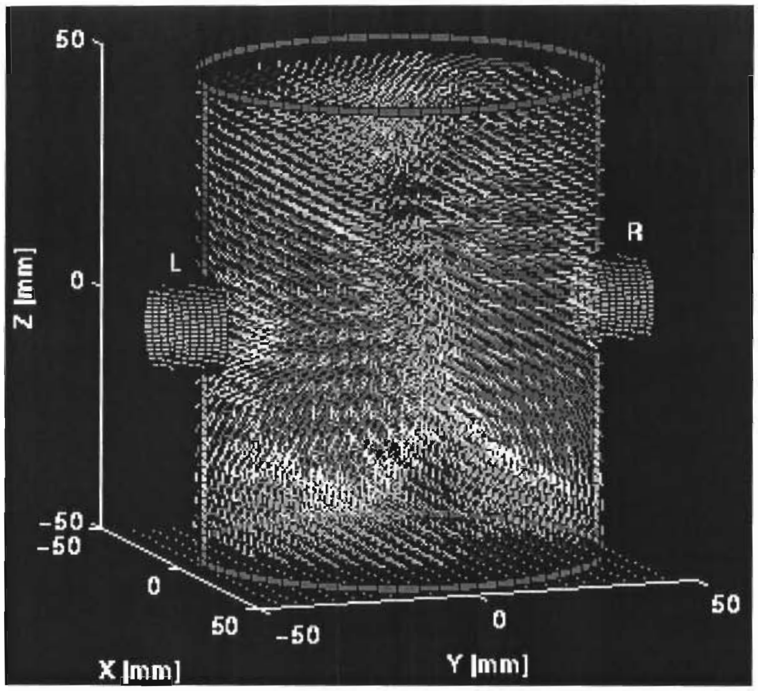

Fig. 2.4 Three-dimensional, time-averaged velocity vectors in the horizontal (xy) plane with contours and surface map of z-vorticity at a Reynolds number of 4,000. [27]

Fig. 2.5 shows one frame of the contours on the z-vorticity component. Zhao and Brodkey directly observed the distribution in both velocity direction and magnitude of the vorticity component by analyzing the vorticity surface. There are four vortices on the z plane, and we can regard them as hills and valleys or positive vortices and negative vortices [30]. The positive vortices or high hills represent plus or counter clockwise vortices. The negative vortices or holes stand for a minus clockwise vorticity.

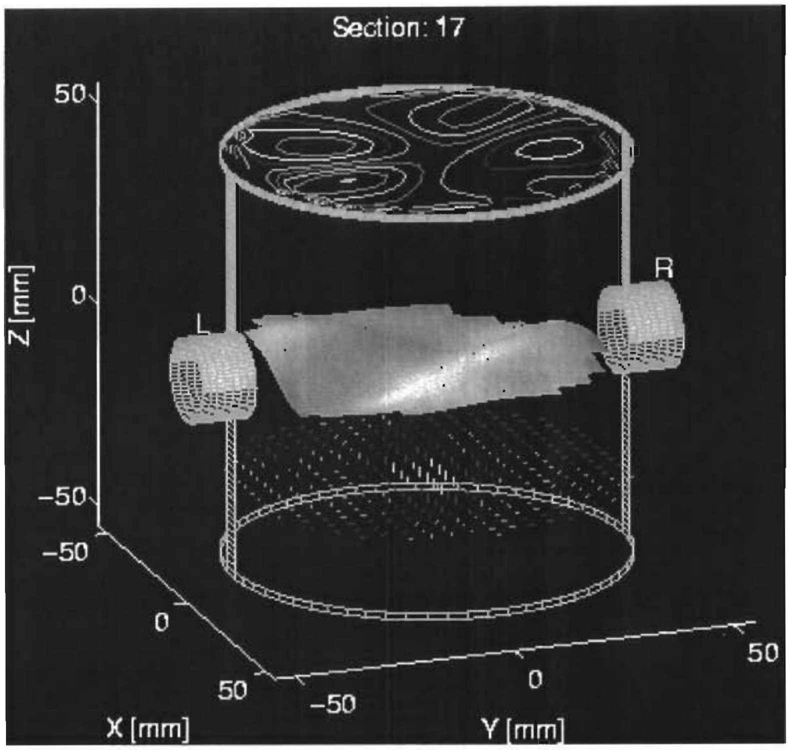

Fig. 2.5 Three-dimensional, time-averaged velocity vectors in the horizontal (xy) plane with contours and surface map of z-vorticity at a Reynolds number of 200. [27]

2.3 Velocity Vectors Measurement Techniques

Velocity vector measurement techniques are the fundamental and first step to understanding the flow dynamics. Through these measurement approaches, laser doppler velocimetry, particle imaging velocimetry, and particle tracking velocimetry, we can derive valuable information about the behavior of the entire flow. This allows us to get a vivid, global, and detailed picture of the physical process taking place in the flow.

2.3.1 Particle Image Velocimetry

Particle image velocimetry is a non-intrusive sheet flow visualization technique that provides qualitative and quantitative information. The goal of PIV is to measure large numbers of vectors over the full field, which will require fast, relatively error-free particle tracking algorithms. The experimental method consists of seeding the flow under study with particles and acquiring the particle image patterns when exposed to pulses of light. The images are then enhanced and processed to determine the coordinates of the particles' centroids in each frame.

Conventional PIV, based on cross-correlation, assumes the velocity to be relatively uniform within a search region and there to be no change in the flow pattern between two consecutive images. The main drawbacks of the cross-correlation method are the difficulty in tracking flows with a high velocity gradient and the need for a high particle concentration. This technique calculates the cross-correlation coefficient between a reference pattern in a first binary image and a possible candidate pattern in the following image. When the velocity gradient is severe, the correlation coefficient between the reference pattern and the distorted pattern obtained from the consecutive pulse can be small. The identification may be missed and may lead to errors. Moreover, a high particle concentration is needed so that enough particles are included in the patterns that the algorithm tries to match in consecutive frames. This high concentration requirement may not be attainable when the resolution of the imaging medium is limited, as in the case of Charge Coupled Device (CCD) digital cameras.

Several parameters need to be considered prior to performing a PIV investigation. The dimensions of the flow facility, type of fluid, and flow velocity range are of great importance and will determine the best setup for the experiment. Experimental parameters include: particle size, density and color, power of light source, duration of the pulses and time separation between pulses, and finally, the magnification ratio for the images. Additionally, depending on the type of flow field under study, a three-dimensional study may be indispensable and may present a larger degree of difficulty than a two-dimensional approach.

PIV replies on scattering particles suspended in the flow to provide the velocity information for the continuous medium (liquid or gas). The accuracy of the velocity field determination is ultimately limited by the ability of the scattering particles to follow the instantaneous motion of the continuous phase. A comparison between reducing the particle size and increasing the particle size to improve light scattering is therefore necessary.

The light that is scattered from the seeds in the flow will be refracted to some extent, possibly introducing another source of error. Flow speed can cause difficulties in tracking particles. If the flow speed is too fast, the cameras will not capture seeds in successive frames. Therefore, error analysis in a PIV tracer-tracking program should be performed using synthetic data.

2.3.2 Particle Tracking Velocimetry

The technique called particle tracking velocimetry is one of the oldest image-based experimental techniques developed by a number of experimentalists. The technique uses small particles as flow tracers located randomly within the domain of interest and analyzes a time series of particle images. In order to observe the motion of the particles, the particle images are multiple images on a single frame or acquired over a sequence of frames with a specific time interval. By proper choice of the particles and fluid (matching density between the particle and the working fluid), the flow tracer particles follow the flow accurately.

The PTV technique is divided into three steps, i.e., image visualization, image capture, and image analysis. The visualization is the most important procedure in PTV. Usually the point-wise particle images at certain times are captured to visualize the velocity of the flow. The particles in the serial images are then tracked to detect the vectors. Particle tracking error in the tracking method may cause numerous erroneous vectors. The second step in PTV is the acquisition of the particle image visualized in the first step. Using a photographic recording, a high-resolution image can be captured. On the other hand, the long series of particle images can be captured by using a CCD camera. However, the type and resolution of the CCD sensor limit the image resolution of a CCD camera. The third step is the analysis of the acquired images. Various algorithms have been developed in order to analyze the particle images, including particle streak images. However, the digital image processing of the particle streak line is not so easy because of overlapping and streak deformation. Also, the digital image processing needs several seconds depending on the algorithms, making real-time analysis difficult. Even if one increases the processing speed, real-time processing of the analysis of the image is still difficult because the realization of parallel processing is difficult. On the other hand, optical image processing has an advantage in terms of processing speed, because with optical image processing one can perform parallel processing at the speed of light. Optical processing is an important topic for real-time flow measurement.

Particle tracking velocimetry is able to follow ("track") each tracer particle along its path, while retaining the position at each time interval. At higher particle concentrations, the particle image overlap in each view is a major contributor to the overall errors in locating particles. It is particularly acute in imaging a 3-D volume. Neighboring particles in the 2-D image plane may actually be separated by large distances in 3-D. Based on Brodkey et al. previous numerical tests to alleviate the errors associated with the partial overlap problem, a threshold for the aspect ratio of the order of 1.5 seems to be an adequate value to detect the suspicious particles. To avoid errors due to particle image overlapping, the use of PTV is usually restricted to low seeding levels [31].

Conventional PTV methods perform well for low seeding densities. The distance a particle travels between exposures is small compared to the average distance to its nearest neighbor.

2.3.3 Hot Wire Anemometers

Hot wire anemometry has long been accepted as one of the most accurate and affordable methods to study velocity fields in turbulent and unsteady flows. Model experimental methods in conjunction with powerful computers for use in data reduction have allowed for the development of probes designed to measure the three components of velocity. HWA is able to provide useful supplementary information on the turbulence characteristics due to the availability of long-time sequences of data. It can measure fluid velocity by sensing the changes in heat transfer from a small electrically heated element exposed to the fluid. The fluids can be air, water or other. The heat transfer anemometer measures mean velocity as well as turbulence. Hot wire anemometry can also measure the temperature, concentration, wall shear stress, and heat flux [32].

A key feature of the thermal anemometer is its ability to measure very rapid changes in velocity. This is accomplished by coupling a very fine sensing element with a fast feedback circuit, which compensates for the drop in the natural response to flow fluctuations as short as three microseconds which can be achieved easily. It is for this reason that the thermal anemometer has become a standard tool for researchers examining the nature of turbulence. The small sensor size, normally only a millimeter in length, also makes this technique valuable in applications where access is difficult or where larger sensors obstruct the flow.

Hot wire anemometry has several advantages such as high frequency response to follow flow fluctuations and transients, high spatial resolution, wide velocity range, relatively low cost, and measurement of other properties such as temperature, concentration, etc. At the same time, the limitations of the thermal anemometry include the following: fragility, sensitivity to contamination, measurements in highly reversing flows and high turbulence flows and output sensitivity to changes in velocity, temperature, and density. Furthermore, the calibration of hot wires in changing thermal conditions (pressure, density, and temperature) makes the technique extremely complex to obtain reliable quantitative velocity measurements.

Hot wire anemometers are also sometimes inaccurate to obtain measurements very close to a solid boundary. Multiple hot wires can be used simultaneously to determine multiple velocity components, but such probes produce more disturbances in the flow field, and the measurement volume becomes large with respect to the smallest turbulence scales. Furthermore, measurements are made at a single point in space. Spatial information would be useful to further understand turbulence.

2.3.4 Laser Doppler Anemometry

Laser doppler anemometry technique is "still widely used today, because it is a relatively low cost method for obtaining velocity data information" [33]. It is well known that LDA generates individual realizations of randomly sampled velocity data because the random arrival of seeding particles in the measurement of volume is nonperiodic. LDA presents some advantages over the hot wire anemometry techniques, such as no flow interference, direct velocity measurement without calibration, and regardless of the velocity field.

The inherent advantages of LDA are "counteracted by discontinuous measurements being randomly distributed in time, by velocity bias due to increasing data rates with increasing velocity, and by inhomogeneous distribution of tracer particles and the error made in the estimation of individual velocities" [34]. All these effects can be considered noise added to the signal. The LDA measurement systems produce signals with a much lower signal-to-noise ratio than do data from modern hot wires. The LDA technique makes it possible to estimate both temporal and spatial structure functions. However, LDA data, like data obtained from other technique (e.g., HWA, PIV), are noise contaminated. This noise mostly derives from the finite size of the measurement volume. Moreover, the velocity time history is reconstructed from random arrival times of the tracer particles. Therefore, the statistics of LDA data is based from both noise and non-equispaced samples.

Furthermore, this technique is quite accurate. Also, current LDA systems can perform three-dimensional velocity measurement at a point. However, inherent in single-point measurements of a flow is the loss of the dimensional interaction occurring in the fluid. As a result, the LDA technique is not employed when investigating highly three-dimensional flow fields, such as turbulent mixing regime.

2.4 Visualization Technique Determination

After careful review of the previous flow field measurements with their respective merits and limitations, the 3-D particle tracking velocimetry (3-D PTV) was selected as the method of choice to probe the characteristics of the opposed jet mixer. The 3-D PTV best suits the requirements for our research purpose. As described previously, the technique has many advantages over conventional measurement techniques such as hot wire anemometry, laser doppler velocimetry, and 2-D PIV. First, full three-dimensional, simultaneous multi-point velocity measurements can be gathered over the volume of interest, proving a wealth of information about the large-scale motions in the opposed jet flow field. Second, by virtue of the nature of the data obtained from the 3-D particle trajectories, the 3-D PTV also provides a Lagrangian description of the temporal and the spatial evolution of the flow field.

Technique	Measurement Characteristics			
HWA	Non-Intrusive	Point	1-3 D	Calibration Problem
LDA	Intrusive	Point	1-3 D	High Temporal Resolution
2-D PIV	Non-Intrusive	Plane	2-D	High Spatial Resolution
3-D PTV	Non-Intrusive	Volume	3-D	Low Spatial Resolution

Table 1: Comparison of flow vector measurement techniques

CHAPTER 3

RESEARCH PROCESS DESCRIPTION AND EXPERIMENT EQUIPMENT

This chapter gives detailed information about the preparation, set up of the experiment, experimental procedures, and analysis procedures. There are four sections included in this chapter: experimental postulate, equipment preparation, experimental procedure, and data analysis procedures.

To learn more about the flow in a typical mixing system, the experimental setup utilized a transparent flow system filled with water, in which small neutrally buoyant flow tracer particles are suspended. The experiment was carried out by using a plexiglass cylinder vessel. The system was gravity-fed to eliminate pulsation, which commonly occurs with pumping. An overflow tank was utilized to provide a constant head source, and the flow rate was measured by two flowmeters at the entrance of the device and by weighting the two outlet flow streams. Flow structures were visualized by seeding the dyed neutrally buoyant particles into both of the inlet streams.

3.1 Impinging Flow System Setup and Operation Procedure

The Ohio State University research on the opposed jet reactor system was first published in 1998 [27]. As shown in the schematic of Fig. 3.1, two inlet jets had the same inlet velocity impinge upon each other in a cylindrical geometry and then flow upward to the outlet.

In Fig. 3.1, the water flow is fed to the overflow feed tank, A, to avoid the effects of pumps and minimizing signal disturbances associated with the pumping of fluid. The two equal flows were driven by the overflow and there were two rotameters at point B to insure both inlet flows were balanced. Because the microcarrier beads may distort the operation of the rotameters at point B, we made sure no particles were in the flow system during the initial setting of the flow rates. The desired overall flow in the system was obtained by the overflow control device, a differential overflow system (C). This overflow system could be moved vertically to provide the desired pressure (Δ h), which could control the flow rate. To maintain the flow, the overflow at A and C is directed to an open tank at D and then recirculated by a small pump at E to the main overflow at A. The two inlet jets met at the center of the opposed jet reactor (F). The outlet of the cylinder provided the input back to the overflow at C.

Experiment Guideline

1. The feed water was first stored at the return system tank D whose volume was 32 gallons, and the volume return tank D should be larger than the volume of the overflow tank A to make sure there is enough water to continue the experiment.

2. The input pumps E generated enough pressure to move the water from the return system tank D to the overflow tank A. There was a small tank inside the overflow tank, which was kept high enough to maintain the pressure head. When the input pump sent enough water into the overflow tank D, the water overflowed the small tank inside the overflow tank D and flowed down to the opposed jet mixer.
3. The two equal inlet flows were directed to the inlets of the reactor shown at F.

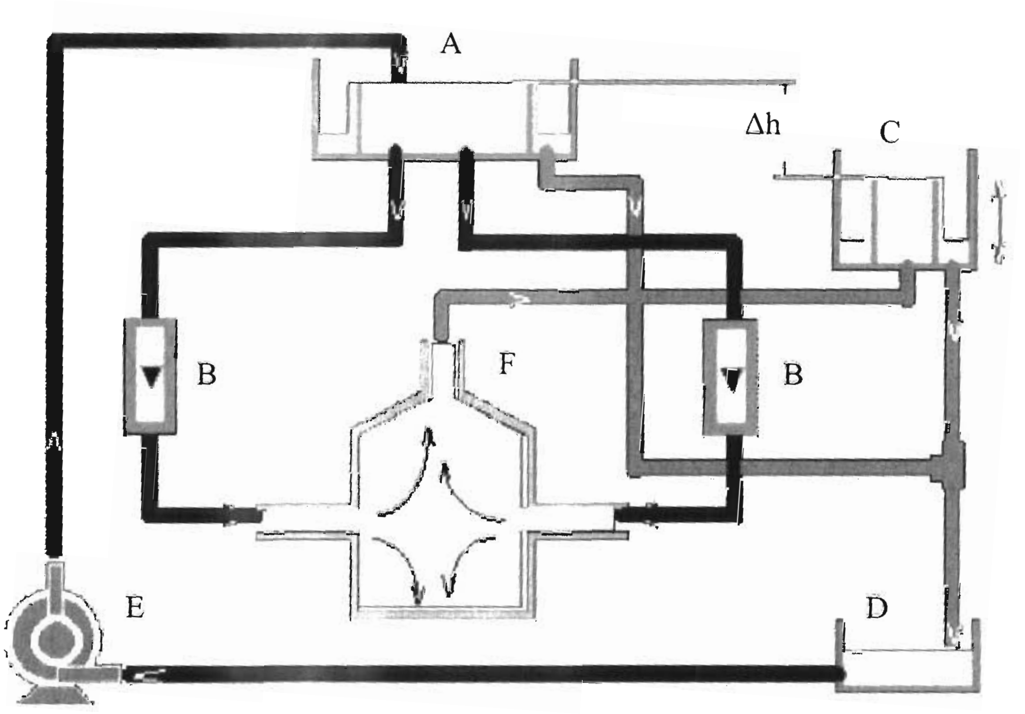

A, C: Overflow control system E: Return pump D: Return source

B: Rotameters F: Opposed jet mixer

The overflow control system works on a deferential height that can be adjusted by the height of tank C.

Fig. 3.1: Opposed jet flow system [27]

3.1.1 Schematic of the Opposed Jet Geometry

In Fig. 3.2 the inlet pipe centerline to the beginning of the conical section was 5.0 cm. The outlet of the cylinder was 6.5 cm in diameter and located at the top of the reactor. There is a conical section between the outlet pipe and the mixer and the height of the conical section was 2.39 cm. The bottom of the mixer was flat and could be moved for later studies where oscillations might be superimposed.

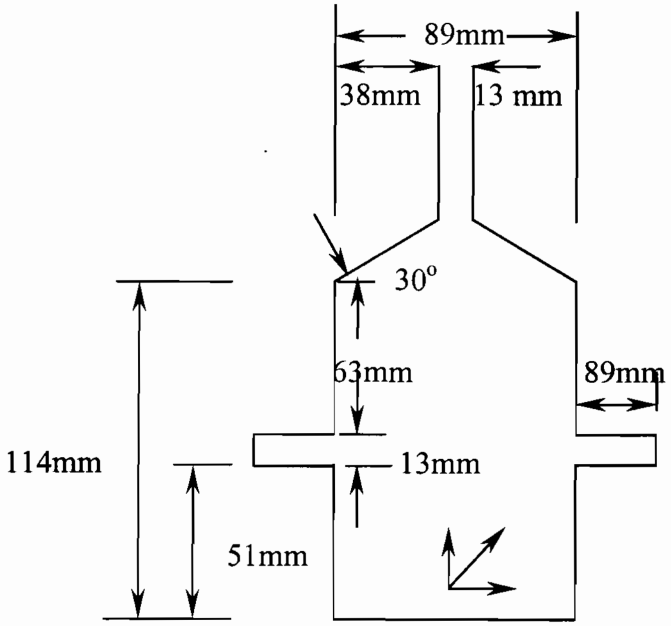

Fig. 3.2: Schematic diagram of the impinging jet system

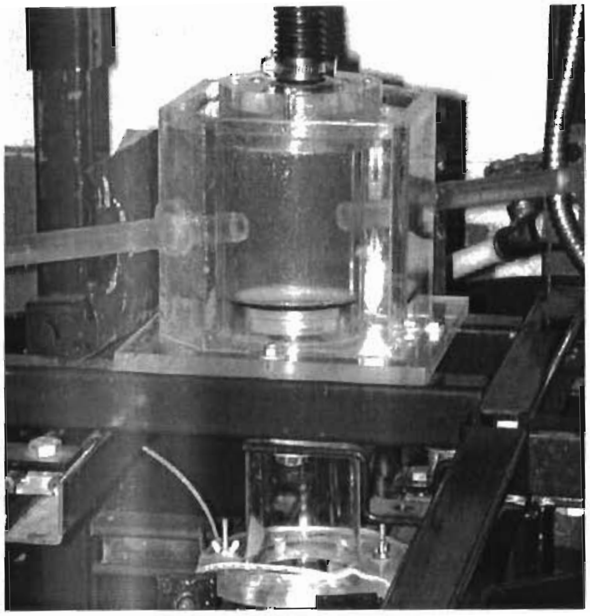

Fig. 3.3: Photograph of the impinging jet system

3.2 Optical Set-Up and Operation Procedure

The optical system consisted of master and slave cameras. In Fig. 3.4, two CCD video cameras (master camera and slave camera) provided two horizontal views at 90°. They provide the flow field as a pair of pictures. These cameras captured the movement of the dyed particles and recorded the particle movements as pairs of image files in the master and slave computers. This system has the advantage the two images are not being condensed onto one frame. While a single camera with a stereo mirror setup can provide similar data, it typically suffers from image overlap between the stereo pairs or a dead spot where image does not appear in the stereo mirror setup. More importantly, the effective spatial resolution is halved.

3.2.1 Illumination Source:

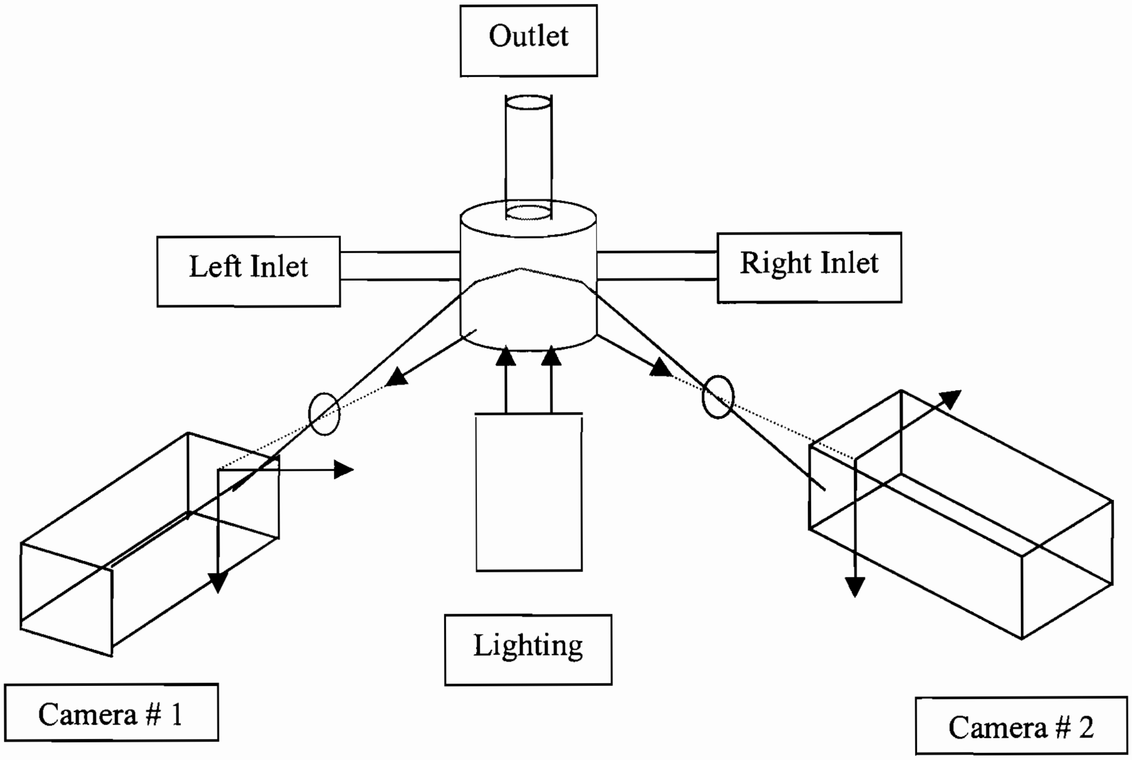

Fig. 3.4: Front view of system with flash lighting and cameras

The accuracy of particle tracking depends highly on the particle image processing and analysis. The importance of top quality raw images for the best final result can not be over emphasized. Various factors such as lighting, image acquisition devices, and choice of cameras contribute to the image quality in many different ways. In our work, the plastic particles had to be dyed so that the particles were clearly visible.

The requirement of volume lighting for the full field image acquisition of the 3-D PTV effectively limited the selection of the light source for the current experimental setup. The idea choice would be a high power strobe light source with a short enough flash duration for the imaging sensor to freeze the motion, and with enough intensity for adequate imaging quality. In the current experimental setup, a Chadwich-Helmuth Strobex lamp strobe light source was selected for its easy integration with an external sync signal and to provide high contrast, frozen images of the particles. For our experiment, the flow field had to illuminated as uniformly as possible when a threshold was selected for particle location identification. Thus a light diffusion lens was constructed of plexyglass to both broaden and diffuse the light beam. The master and slave cameras had electronic controlled shutters, which were kept open during our experiments without blurred images.

In Fig 3.4, 20.32 cm beneath the opposed jet cylinder, a Chadwich-Helmuth Strobex 270D lamp strobe with pulse width for the strobe only 10 ms was installed as a lighting source. The high 10,000 volts Strobex lamp strobe light source produced enough intensity for good contrast in dyed particles in the working fluid, water.

3.2.2 Indoor Preparation

Room temperature was not controlled but did not change over the time of the experiment. For PTV analysis, the flow field was illuminated as uniform as possible because our stereograms analysis software used the gray level and particle location to identify the particles. In other words, by using different gray level, we could figure out different particle numbers and of course the difference in particle amount may or may not be the particles themselves because some of the contributing particles may have been the background noise. Also the software used maximum and minimum particle distances to help avoid false tracks. If two particles were so close that their distance was smaller than the maximum particle distance or the particles are partially overlapped and they had enough thresholds, the software would conclude both particles but in fact there was only one big particle. So how to determine the apposite gray level and particle distance was one of the most important issues in our research.

3.3 Experimental Hardware and Software

The development of relatively inexpensive digital cameras and digital computers as well as the development of elaborate software has now allowed us to develop techniques to extract full field quantitative information from particle flow visualization images. To draw from the advantages of flow visualization and provide quantitative information about the spatial structure of the flow, MV-1000 μ –Tech Corp. boards and in house particle identification software were utilized. Zhao wrote the Windows based image process software in Borland C++™ and Matlab ™ to support image acquisition, video adjustments, file storage, particle identification, particle tracking, particle velocity calculation and much more. Details of such methods can be found in Zhao and Brodkey [28] and Guezennec et al. [35].

3.3.1 Processing Hardware

Two Gateway-PC^{TM} computers (the master and slave computers) were running the Windows 98^{TM} operating system. The two computers (1-gbyte ram each) performed the bulk of the 3-D PTV acquisition and calculations. The tasks included the image acquisition and digitization, the determination of 2-D particle image positions, the 2-D tracking for each side of the stereo images, and the 3-D stereo matching, as well as all the overall task of control. For image data archival, a 12.6 GB hard disk was installed in each computer. The maximum number of images to PC memory was 2,000 for the Gateway PC, 1-gbyte-ram computers. Before we started capturing the sequence, we needed to set up the recording options according to our requirements, and then started the video recorder to capture a sequence of frames. After a sequence was captured, we could play it back from the system memory or hard disk. Finally, the sequence which was captured to memory disk could be saved, so that we could open and playback it in the future.

3.3.1.1 CCD Cameras

Haam and Brodkey used a mirror system to reduce the initial cost, simplify the optical system, and eliminate the synchronization issues present in dual-camera systems [5-6]. But the disadvantage is that the two views are on one frame. The two-mirror system had its disadvantages in size resolution. Compared with the previous optics system, the new optics recording system was composed of two CCD video cameras and divided the flow field into a pair of pictures in the time domain.

The image acquisition system utilized two PULNiX TM-6701AN square pixel, black and white full-frame shutter cameras with asynchronous reset, non-interlace double-speed scanning VGA format (30 Hz), two-row scanning (120Hz), and partial scanning (100 and 200 lines) capability. The CCD imager of the TM-6701AN was used at a 30 Hz (1/30 second) frame rate. This feature provides high sensitivity for dark environment applications. This progressive scan cameras free users from the constraints of traditional television scanning system, permitting full vertical frame electronic shuttering a very high resolutions. The PULNiX CCD camera also has a partial scan mode, with capture rates from 30 to 200 frames per second. In our experiment, the cameras were set at 30 frames per second with 648H×484V pixels of resolution.

The two CCD video cameras were placed facing the opposed jet mixer. In Fig. 3.4 and Fig. 3.5 the two stands were joined together to create a 90° angle between the two cameras. During the experiment operation, no changes could be allowed. Even if there was even a small change, the whole image geometry will change and the velocity vector and vector position will not be correct.

3.3.1.2 Optics Recording Equipment

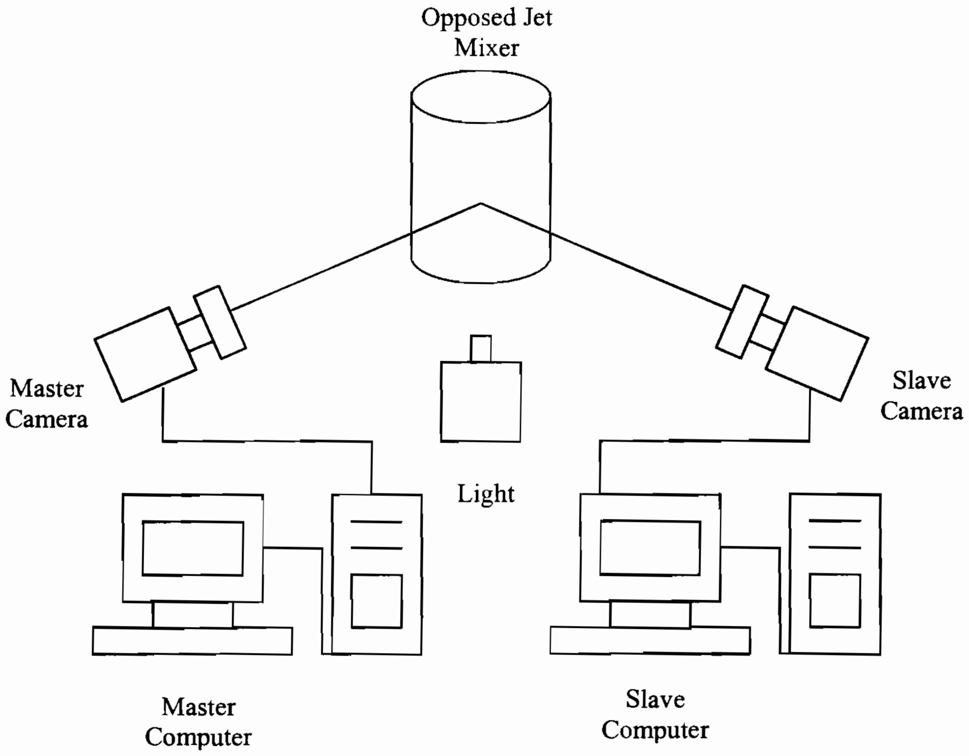

Fig. 3.5: Front view of recording equipment and analysis equipment

The 3-D PTV requires a sequence of stereo image pairs to extract velocity information. For the best results with the 3-D PTV, the desirable separation angle between the stereo views is 90°. This is best accomplished with a dual camera system.

Both the master and slave CCD cameras have the same characteristics. From Fig. 3.4 and Fig. 3.5, the data was recorded in Pulnix CCD video cameras at a 30-Hz rate, which is adequate for our study. The resolution of the CCD camera is 648H×484V pixel array running in an interlaced mode at a full frame rate of 30 Hz. Once the data were on computer and could be replayed, the image processing and analysis were fully automated.

3.3.1.3 The Tracking Particles

Pylakrome yellow was used to dye the particles. These dyed particles were tracked by visual observations so that they did not gather at the top or bottom of the tank, but kept well distributed throughout the volume. The particles have a very uniform density that simplified the density matching. Particle size is also critical. A suitable choice of tracer particle size should be made depending on what flow characteristics are to be studied.

To make sure the particles all follow the flow motion, the particles should be small and light enough. But at the same time, for the visualization devices to trace the particles, the particles should be large and bright. The dyed plastic micro carrier beads (SoHill Engineering, Inc.) were used as tracer particles. The microcarrier beads were first dyed by the pylakrome yellow dye in a solution of toluene and methyl alcohol. The plastic particle size ranged from 150 μ m to 200 μ m and the specific gravity was 1.02. The flow was maintained for another period of time to ensure that the particles were well distributed before the measurement experiment began. For the purpose of dynamic measurements, the gravity of the tracer particles should be as close as possible to that of the working fluid.

The process of dying microcarrier beads:

1. Make 100 ml. of toluene solution
2. Make 10 ml. of methyl alcohol
3. Calculate weight of dye at concern of 4~8 oz./gallon ~g/100ml (3g/100ml)
4. Mix two solutions and dye together in the conical flask
5. Place the particles in a shaking shaker and leave them for one day
6. After particles are dyed, vacuum filter toluene, and collect particles on a Whatman™ filter paper
7. Let particles dry in the hood to remove all toluene

In our experiments once the flow was established and maintained for a period of time, the bypass lines were opened and the rotameters were closed. At this point, the flow makers were mixed into the system at tank D. The flow was also checked at the exit of pipe D.

3.3.2 Processing Software

The image computer-recorded files were processed by the image acquisition function using two image capture boards (μ-tech MV-1000), which were installed in two computers respectively. The Pulnix CCD video camera was controlled by the MV-1000 Grab Sequence Application Version 1.3 (Mu Tech Corp. 1996 & 1997). The MV-1000 is a PCI bus image captures board, which allows the MV-1000 to transfer live video to either the system VGA card for display or system memory for processing.

3.4 Experimental Procedure and Apparatus Setup

This section below describes in detail the operation procedure, software analysis procedure and other additional procedures, which are all essential parts to achieve our experimental results.

3.4.1 Threshold Preparation

For PTV work, the flow field was illuminated as uniformly as possible and a threshold was selected during particle location identification. Even after the background subtraction, there could be non-uniformity in the new background of the image. For example, in the final image to be analyzed, if the threshold was selected below the background in a sub-region of the field, the entire sub-region would look like a very large particle (larger than the maximum allowed) and thus that sub-region would appear without particles. To avoid this problem, the background was established from a blank picture without particles. The threshold was set to this level and was tested using a picture with particles. The threshold could often be reduced a little; unit-by-unit, but this must be checked for each step to make sure that blank region is not introduced.

3.4.2 Steps Undertaken in the Experiment

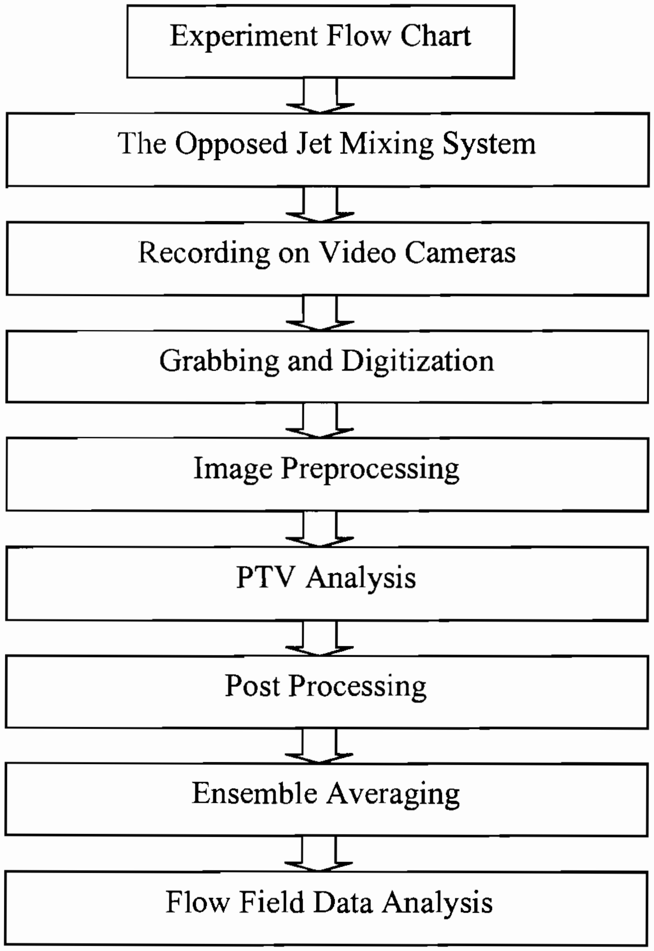

Fig. 3.6: Flow chart for experiment process [27]

Experiment Guideline

1. First, the three-dimensional imaging system was set up, which divided the field into two horizontal views at 90° and generated into a pair of pictures in the time domain using two standard 30 Hz CCD video cameras.
2. The flow field velocity vectors were recorded as image files on the CCD video cameras. The data were recorded as master and slave image data files on master and slave computers.
3. After pre-processing of the raw images for image quality standardization, we began to grab and digitize the image data. The images were converted into numerical representation grid files and were transferred into the digital computers. The final data were 648H×484V nominal resolution at 30 Hz.
4. By using the image processing and analysis tools, the moving particles in the image files were removed from background and were further processed.
5. By using PC based PTV analysis software, the data files were translated into Microsoft Word^{TM} format, which contained the vectors' 3-D coordinate position and velocity data. The software furthered 3-D particle tracking by setting the gray level and the max particle distance.
6. Both master and slave Microsoft Word^{TM} formatted grid files were added together by 3-D matching. The 3-D position and velocity at randomly identified spatial locations were recorded at the flow volume.
7. The adaptive Gaussian window (AGW) filtering technique processed the validation of the velocity vectors. The post processing analysis used AGW interpolation to interpolate the results on regular grid files. The AGW filtering rejected the velocity

vectors, which were too different from their neighborhoods. Velocity calculation and 3-D drawing and were also available for displaying.

8. Finally, the data visualization and analysis step illustrated, posted, the surface and animate data in both 2-D and 3-D in very large data sets. Data were explored from many different perspectives and sections so that all the patterns and relationships in the data were seen.

3.4.3 Detailed Software Analysis Procedure

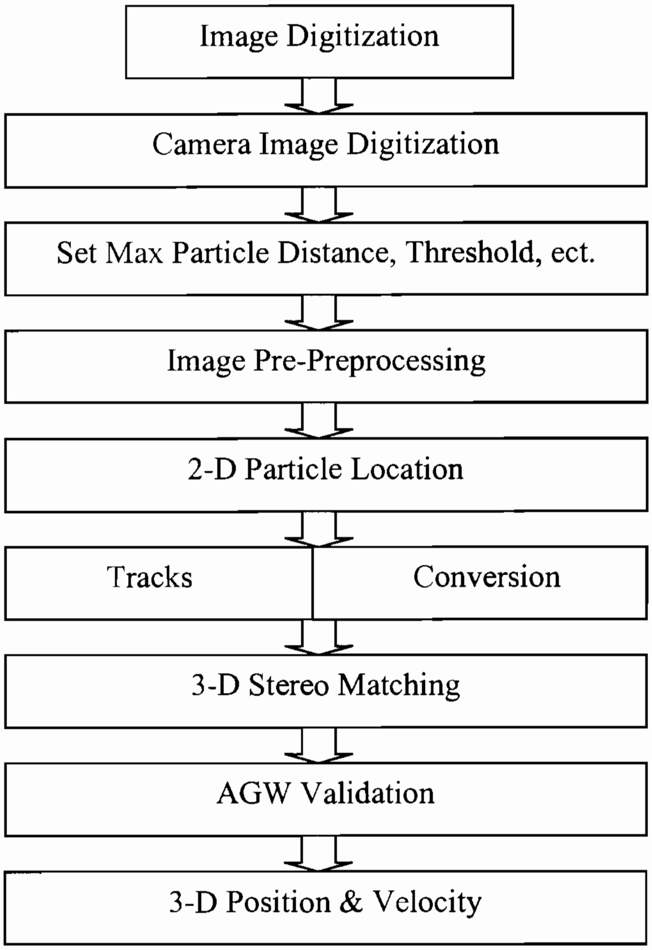

Fig. 3.7: Flow chart for code process [27]

3.4.4 Grabbing Images Software Digitization Procedure

After the image acquisition, a code for a 3-D PTV was developed to extract three-dimensional velocity fields from time sequences of singly exposed stereo images of flow tracer particles. The CCD video cameras were controlled by the MV-1000 capture board, which is an excellent solution for interfacing to the new generation of high-speed digital cameras. The MV-1000 digitized standard or non-standard analog camera video into 8 bits per pixel at rates 40 million samples per second. The digitized video was stored in on-board VRAM or transferred in real time to system memory and/or the VGA card for processing. When old images were still in memory, we needed to clear memory, which would empty the memory of all previous images. With the current PC's 1 GB memory, this allowed slightly over 2000 (684x484 pixels) full size frames to be taken.

Operation Guideline

1. Selected a non-standard camera by loading a camera configure file.
2. Set up the appropriate maximum grab size, maximum and minimum particle distances, and gray level.
3. Specified in the camera configure file as the frame size, or subsampled the video image, by changing the frame size or scale at this time.
4. Adjusted the CCD video cameras to capture the mixing characteristics, and played it back from the computer memory.
5. Saved the captured sequence to hard disk in order to process and playback in the future.

3.4.5 Determine Threshold and Particle Distance Parameters

After the images digitization, the pre-processing of raw images (such as background subtraction, contrast enhancement, and filtering) was done. Thresholding was one of the most important approaches to image segmentation. The selection of threshold was done manually after various comparisons were made at different threshold levels by verifying particle images identified by the software with those appearing on the computer screen. Table 3.1 shows the vector numbers gained by setting different maximum distance.

Max Distance	Vector Number	Max Distance	Vector Number
0.063 cm	787,080	0.063cm	857,649
0.083cm	738,145	0.083cm	821,828
0.1cm	857,649	0.1cm	787,080
0.126cm	812,828	0.126cm	738,145

Table 3.1: Vector numbers gained by different maximum distance

In general, the particle distances were not large among all four maximum distance levels. When comparing with the big vector number differences that occurred when gray level = 35, gray level 50's vector number was 15%-20% higher than threshold 35's vector number. At last, we chose gray level = 50 and max distance = 0.1cm which we thought could best reflect the flow field.

Because we had master and slave CCD cameras, after every experiment there were 2,000 images data files in both the master and slave machines. We put them in the directory of PTV image process software to generate 2,000 velocity files, which were associated with the master and slave files. The usage of interpolation function generated 2,000 grid files, which was processed by the Matlab™ conversion package and desired the flow vector images.

3.4.6 Image Pre-processing

The flow field images taken by CCD cameras were digitized on master and slave computers. Image processing was performed to facilitate the task of locating particles. Image pre-processing was the image enhancement step used to improve the digitized images prior to the particle identification and tracking process. This step is always important to enhance the raw images that needed corrections due to experimental limitations. Image techniques were used after an image was obtained. They were divided into two categories: image processing, which concerned with the process of the velocity vector images from image acquisition, and image analysis, which is the task of obtain useful information from an image. The goal of the image processing part of research was to generate an image simple enough so that the computer can identify and locate all the particles in it without any ambiguities. The goal of image analysis section was to identify and locate the particles in the already processed image, match them in pairs between two successive images, and calculate their velocity vectors. The pre-processing step enabled us to change identification particles parameters, obtain particle locations, and track particles. So we could obtain an average image and subtract this image from each of the raw images. The average image could be viewed on this paper. We also were able to use the internal video viewer panel to look at all of the images currently stored in the PC memory.

3.4.7 Image Background Subtraction

Background subtraction means separating the particles from the background (image segmentation). Background subtraction is the process that subdivides an image into its constituent parts or objects. Segmentation is one of the most important elements in automated image analysis because it is at this step that objects or other entities of interest are extracted from an image for subsequent processing, such as description and recognition. Image segmentation consists of dividing the gray scale into bands and using thresholds to determine regions or to obtain boundary points. The subtraction was performed by thresholding the images with a value obtained from our previous gray level comparison. The averaged image could be subtracted either from the images stored in the PC memory or from the images in the hard disk. After setting up the gray level, the program would assume that the light points whose thresholds are less than the assumed gray level number were background. And after figuring out the particle position and velocity vector, the program would begin to subtract the mixer background from the original images. The total number of images to be subtracted was 2,000 in each data set. The subtracted images would replace the original images in the PC memory. The original image files were replaced and overwritten after this subtraction operation. After this subtraction operation, the remaining parts in every image file were only the particles.

3.4.8 Determination of 2-D Particle Positions

Image digitization is required prior to any digital image processing. It discretizes a physical scene into small picture elements and at the same time converts continuously varying degree of brightness into a discrete gray level for each pixel. Electronic image sensing devices such as the CCD cameras were used in this process together with image frame grabbers to transfer the converted signal from the image sensing devices to the computer in a digital grid form.

Particle image separation from the background can be considered as an image binarization process. This means that the digitized image pixels can be segmented into two groups, one belonging to the particle images and the other belonging to the background. While the task is quite straightforward, the actual process requires careful considerations for various imaging scenarios. We would gain the positions of each particle in the 2-D image plane.

Once a threshold value was determined, the images were computationally analyzed by grouping all the pixels (interior and boundary) belonging to a given particle. A particle here was defined as an arbitrary shape connected with a set of pixels. This information was then used to compute intensity-weighted centroidal coordinates and size of the particles and was also used to compute intensity weighted second-order moments of area to estimate the aspect ratio and orientation of the particles.

3.4.9 Image Analysis Program 2-D Tracking

Having reduced the images to a set of 2-D particle positions, the second module used a sequence of frames to establish the most probable particle path (position versus time) for each particle. In order to combine the master and slave image files together, we used the fluid field and velocity vector programs, which were written by Borland C++^{TM} to match the master and slave files. The 2-D tracking function was applied by examining the maximum displacement of particles between consecutive frames and it was measured in percentage of image size. The parameter was used to limit the range tracked so that excessive tracking times were encountered. Maximum error was to guide the program to find the best 2-D tracking which was the maximum displacement of particles between three through five consecutive frames. 2-D tracking used maximum error as a continuity criterion to insure that determined tracks were reasonable and not out of bounds with regard to acceleration. If the maximum error between three frames were satisfied, then four frames were considered, etc. This was done separately for each of the two views. In other words, 2-D tracking is performed for each view.

3.4.10 Image Analysis Program 3-D Matching

The third step of the algorithm was to perform stereo matching: reconstructing the 3-D coordinates from two 2-D projections. The stereo matching step could be carried out by matching the individual particles in two views. Same as 2-D tracking, we first needed to combine the master and slave image files together and delta T, which was between two consecutive frames as established by the video system. The particles whose centers overlap were matched first and removed from the list. Then a search area equaled to the radius of every individual found particle was formed and the search for its match was carried out in that area in the generated image. This was done by the remainders, which were not matched found particles. If there still were particles not matched after the second search, a third search would start trying to match the remaining generated particles with found ones. For stereo matching, a limitation was needed on the vertical displacement of a particle observed in two views. Ideally, if the camera positions and all optics were perfect, the displacement would be zero. "Max dy" was the maximum difference in the 2-D tracks in height between the left and right images. Just as in the case for 2-D tracking, there was a penalty function for stereo matching. This penalty function was done in the 3-D domain to track the particles that did not lie below the maximum distance and discarded as not being smooth and continuous.

3.4.11 Adaptive Gaussian Window (AGW) Validation

After the stereo matching algorithm reconstructed the best 3-D tracks from the 2-D tracks, a final validation of tracks (position and velocity) was performed in the last module by means of an automatic validation process based on adaptive Gaussian window filtering. In this module, neighboring velocity vectors in the 3-D sense must be relatively similar if the data density is sufficiently high with respect to the spatial scale of the flow. To evaluate this relative similarity, each velocity vector was compared to a smooth local 3-D interpolated value, calculated with a 3-D Gaussian filter. If the actual velocity vector was too different from its neighborhood average, in other words, if the vector in the square box was very different from its original value, it was rejected as being possibly erroneous. This process was then repeated by advancing the frame count by one. In this fashion, new tracks were independently established at each time step and the procedure was continuously self-starting and self-terminating. This was important for the open flow system where particles move in and out of the image volume.

3.4.12 Average Image

After first generating and displaying the images, we could average images. The raw images could be in the PC memory or in disk files and were needed in order to read images from memory. In the first 18 data sets, there were 2,000 images in each data set. The last set had 2,300 individual frames in set 18). In our 11-frame moving average process, the sequence was averaged over 11 continuous images. The frames are then shifted by one frame forward. The process is repeated. This created a moving window average. The software generated 2,000 grid files, which were processed in the Matlab^{TM}, and the dynamics graphic interchange format (GIF) files were generated.

3.4.13 Matlab^{TM} Conversion

After the grid data files were generated, a Matlab^{TM} program was available to read the velocity vector grid files and acquire the vectors' coordinate locations and converted the particle location files to the image files.

3.4.14 Image File Types Conversion

This is a small but powerful DOS^{TM} program. By setting up the image file name and number of image files, the program could change the image file type from GIF format to JEPG format because the GIF format files with 24-bit color were large compared with the JEPG format files, which have 8-bit color. This step enabled the hard disk and memory to store more images files.

CHAPTER 4

STATISTICAL CALCULATIONS AND COMPARISON OF THE VELOCITY VECTOR DATA

The first task was to establish initial condition for latter computation efforts. For this, to evaluate the accuracy of our experimental data, both the continuity equation and Taylor's hypothesis were used to determine the $\partial U_x/\partial x$ term. In this chapter, the results are systematically and statistically examined and compared. A computer code was written to calculate the $\partial U_x/\partial x$ term by using the continuity equation and Taylor's hypothesis to gather other useful information. The results were saved as a grid file format for further research using CFD techniques.

4.1 Computation by the Continuity Equation and Taylor's Hypothesis Methods

The code solves for $\partial U_x/\partial x$ term by using the three-dimensional incompressible continuity equation and Taylor's hypothesis. The structured 21^3 grids were used. We need the boundary conditions on all surface and initial conditions at $t = 0$ for use in DNS and LES computation. The goal here is to obtain best experimental averaged data to determine the initial conditions for latter computational effort. In our opposed jet mixer experiment, the boundary condition and initial condition are:

Boundary condition: $V_{boundary} = 0$ at $t = 0$ (Near wall velocities are zero)

Initial Condition: Re = 2,000 at $t = 0$ (Constant pressure head tank)

$$\partial\rho / \partial t + (\nabla \cdot \rho U) = 0 \tag{3.1}$$

Where:

ρ = density

t = time

$\nabla = i\frac{\partial}{\partial x} + j\frac{\partial}{\partial y} + k\frac{\partial}{\partial z}$

U = stream velocity

The material (water) is incompressible, constant density; the continuity equation reduced to the continuity equation for incompressible flow.

$$(\nabla \cdot U) = 0 \qquad (\nabla \cdot U) = \frac{\partial U_x}{\partial x} + \frac{\partial U_y}{\partial y} + \frac{\partial U_z}{\partial z} = 0 \tag{3.2}$$

Where:

$\nabla \bullet U$ = divergence of the velocity

x, y, z = directions

$U_{x,y,z}$ = velocity in x, y, z direction

The CCD cameras were used at a 30 Hz frame rate. The reduced data for velocity had for each frame 21^3 points with $\Delta t = 1/30$ sec. The first way is to determine $\partial U_y/\partial y$ and $\partial U_z/\partial z$, and use the continuity equation to calculate the $\partial U_x/\partial x$ term. The second way is to calculate $\partial U_x/\partial x$ by using Taylor's hypothesis in Fig. 4.1. Also Taylor's hypothesis is needed for$\partial U_y/\partial x$ and $\partial U_z/\partial x$. In Taylor's hypothesis, U is a constant velocity of the flow field. U can be the overall velocity of the 21^3 points or it also can be the average velocity at each point. The overall velocity does not make sense because there are both positive and negative velocities involved. In our calculation process, we used the average velocity at each point in the Taylor's hypothesis, but did evaluate the overall velocity approximation.

The $\partial U_x/\partial x$ term can be evaluated using the rearranged continuity in equation 3.3 and Taylor's hypothesis in equation 3.4. Therefore, we can evaluate the two results to check on how good the Taylor's hypothesis is the average.

$$\frac{\partial U_x}{\partial x} = -\frac{\partial U_y}{\partial y} - \frac{\partial U_z}{\partial z} \tag{3.3}$$

$$X = U \times \Delta t \tag{3.4}$$

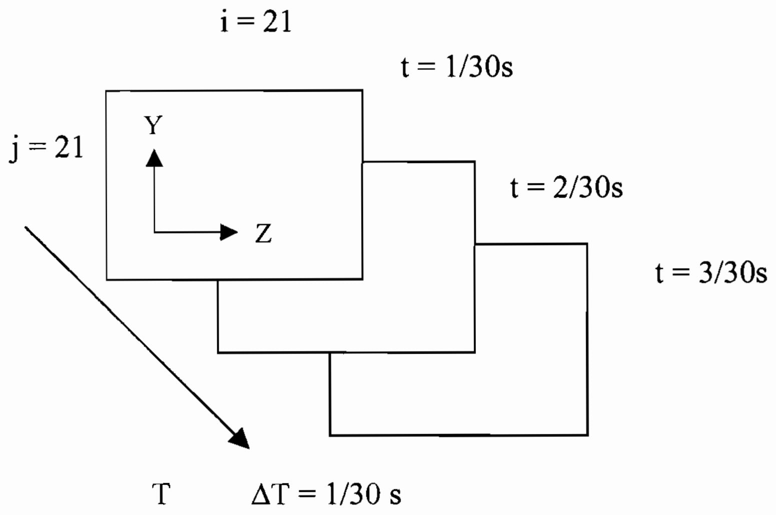

Fig. 4.1 Taylor's hypothesis theory

4.2 Numerical Differentiation of Equally Spaced Experimental Data

The best estimate of the derivative at every experimental point is "to fit a function to several experimental data points on both sides of the particular point and then difference the resulting function analytically at that point" [36]. Polynomials are the most useful functions for approximations. Polynomial approximations are of three general types:

1. Least squares approximations where the sum of the squares of the differences between f (x) and its approximations is minimized over a discrete set of points.
2. Interpolation approximations, of which Newton's interpolation formulas with divided differences and Lagrangian functions, are two of many examples.
3. Minimization of the maximum error approximations.

4.3 Least Squares Power Functions

The least square analysis in equation 3.5 and equation 3.6 are assumed to represent the data. For this case Equation 3.5 is simplified into a power series by equating P_j (X) to X^j [37].

$$f(x) = \sum_{j=0}^{m} \alpha_j P_j(X) + \varepsilon \tag{3.5}$$

$$f(x) = \sum_{j=0}^{m} \beta_j X^j + \varepsilon \tag{3.6}$$

Where:

x = independent variable

f (x) = dependent variable

m = degree of the polynomial

α_j = i^th polynomial coefficient

P_j (x) = some as yet unspecified function of the independent variable X and is of degree j

β_j = power coefficients

ε = error which is independently distributed at each point

4.4 Smoothing

Our experimental data require smoothing before differentiation is performed. Smoothing consists of passing a least squares polynomial through the data points in order to determine α_j and the constants in P_j (x) and then replacing f_i with the generated function Y (X_i). The best method is "to select a small, odd number of points, evaluate Y at central point, and proceed using the movable strip technique" [37]. In our smoothing process, 11 was eventually chosen as the small, odd number.

4.5 Selection of Number of Points and Degree of Fit in Each Strip

There is no known test to assist in the selection of N, which is the number of data points to be included in each strip. A three-point formula is unsatisfactory for experimental data, because a second-degree polynomial fits all three points exactly. A five-point polynomial works well "when the data are not too bumpy, whereas a nine-point or higher polynomial may be required for data with large errors, even after smoothing" [37].

4.6 Numerical Differentiation of Equally Spaced Data

4.6.1 Smoothing Formulas

Orthogonal polynomials are the most convenient for evenly spaced data. The most useful smoothing formula is the third-degree seven-point. Table 15 in the appendix supplies the coefficients for smoothing formulas to use in Equation 3.7.

$$Y_s = \frac{1}{D} \sum_{i=-s}^{i=s} (C_i f_i) \tag{3.7}$$

Where:

D = constant

C_i = constant

f_i = dependent variable

s = translated independent variable

For the third-degree of polynomial and seven-point case, equation 3.7 is simplified into equation 3.8:

$$Y_0 = \frac{1}{21}(-2f_{-3} + 3f_{-2} + 6f_{-1} + 7f_0 + 6f_1 + 3f_2 - 2f_3) \qquad (3.8)$$

Where:

Y = approximation of f, calculated from in the case of equally spaced data

f_i = dependent variable

4.6.2. Sloping Formulas:

After the data have been smoothed, N and m are selected and the suitable formulas applied. Table 16 in the appendix supplies the coefficients for the more commonly used sloping formulas to be used in Equitation 3.9.

$$\frac{dY_s}{dX} = \frac{1}{Dh}\sum_{i=-s}^{i=s}(C_i f_i) \qquad (3.9)$$

Where:

D = constant

C_i = constant

f_i = dependent variable

s = translated independent variable

h = spacing in equal-spaced independent variable

In the third-degree of polynomial and seven-point case, equation 3.9 is simplified into equation 3.10:

$$\frac{dY_0}{dt} = \frac{1}{252 \times \frac{1}{60}}(22f_{-3} - 67f_{-2} - 58f_{-1} + 0f_0 + 58f_1 + 67f_2 - 22f_3) \qquad (3.10)$$

Where:

Y = approximation of f, calculated from in the case of equally spaced data

f_i = dependent variable

h = spacing in equal-spaced independent variable, X_{i+1}-X_i

4.7 Computation Code by Using the Continuity Method and Taylor's Method

A Matlab computer code including the continuity equation method and Taylor's hypothesis method was composed to obtain derivatives of functions representing the experimental data. The flow chart in Fig. 4.2 illustrates the whole steps of calculation for the 11-point time average and 7-point polynomial case. The 11-point time average was selected because this gave a 30 Hz time sequence that looked (visual) smooth to the observer. The selection of the 11-point average (as opposed to 7, 9, 13, etc.) will be discussed latter.

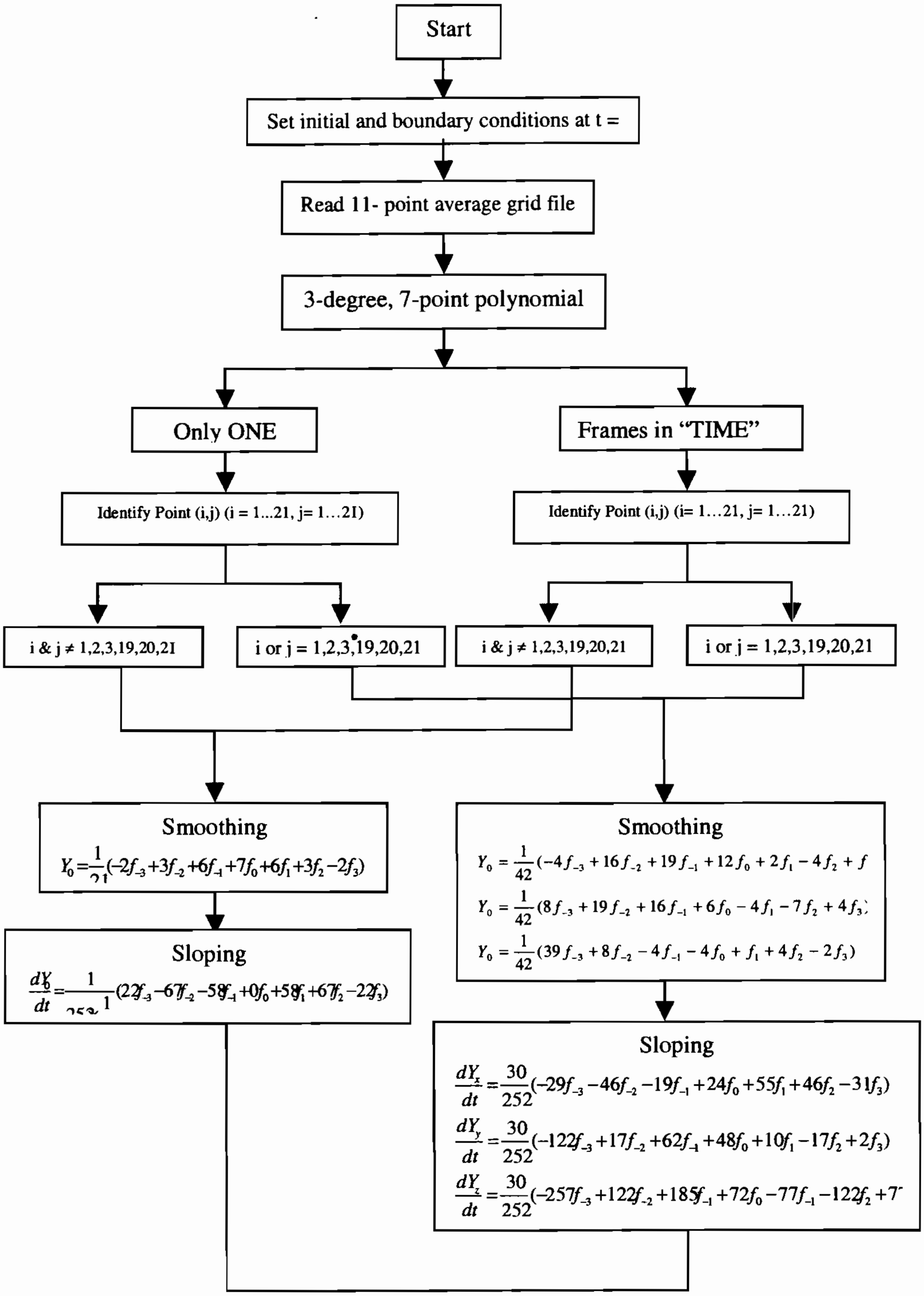

(Continued)

Fig. 4.2: Matlab^{TM} program flow chart

Fig. 4.2: Matlab™ program flow chart (Continued)

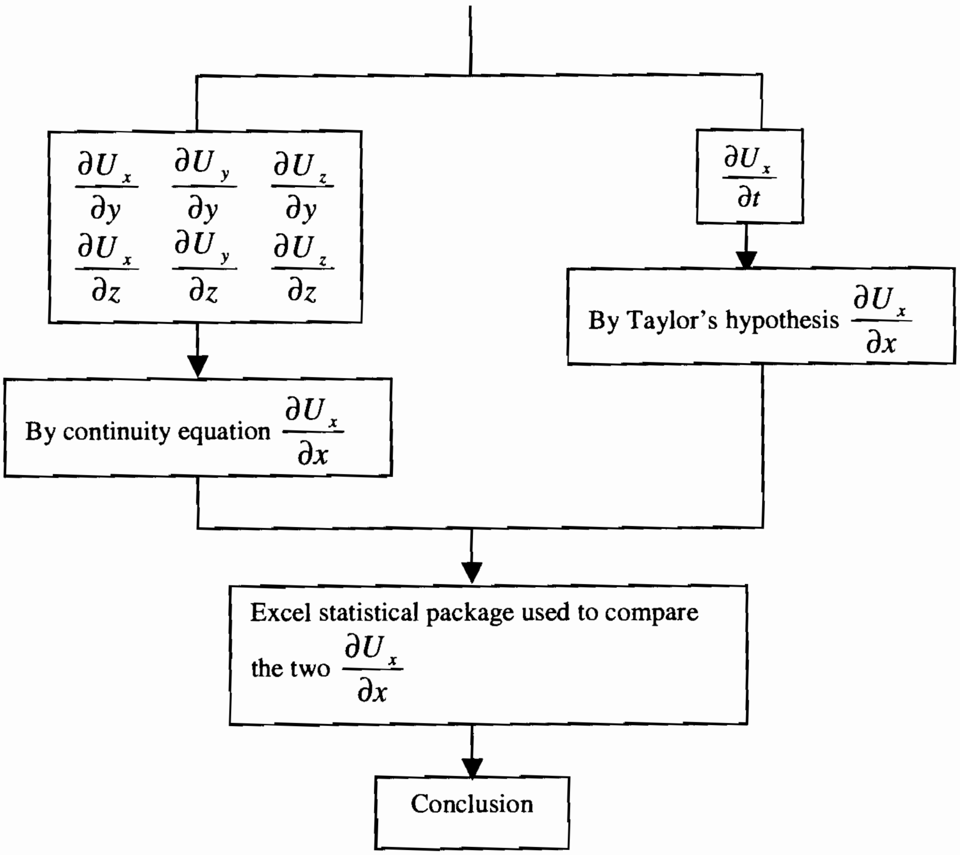

4. 8 Statistical Analysis Between the Continuity Equation and Taylor's Hypothesis Using $U_{\text{local velocity}}$ and $U_{\text{overal velocity}}$

Statistics is concerned with making deductions from a sample of data about the population from which the sample is drawn. The F-test is widely used for comparing different estimates of variance. Statistical T-test is that of comparing the means of two samples of data. In the Taylor's hypothesis, the $U_{velocity}$ term can be either $U_{local\ velocity}$ or $U_{overall\ velocity}$. $U_{local\ velocity}$ is expected to be better and is the mean velocity on each point of 21^3 flow field and $U_{overall\ velocity}$ is the average velocity over the entire field.

4.8.1 Comparision Between Continuity and Taylor's Hypthesis Using $U_{local\ velocity}$

After reading original gird files, the Matlab program calculated $\partial U_x/\partial x$ by using the continuity method and Taylor's hypothesis method by using $U_{local\ velocity}$. The two $\partial U_x/\partial x$ results are at the initial condition. Table 3.2 shows the statistical summary of two methods.

Microsoft Excel's produced summary statistics for the continuity method and Taylor's hypothesis method given in table 3.2. To gain a deepper understanding of the results and test the Taylor's hypothesis, we can use the F-test and T-test to test whether the two $\partial U_x/\partial x$ results are different at a given confidence level. The null hypothesis in our case indicates that there is no difference in these two $\partial U_x/\partial x$ results by using the continuity method and Taylor's hypothesis method. F-test generates a report of univariate statistics for data in the input range, providing information about the central tendency and variability of our data. In table 3.3, $F_{statiscal} < F_{cririsal\text{-}one\ tail}$, which indicates that the two variances are not equal. Next we use T-test assuming not equal variance, which means this T-test form, assumes that the variances of both ranges of data are equal; it is referred to as a heteroscedastic T-test. By using a T-test assuming unequal variance, we determined whether two sample means are equal or not. From Table 3.4, it is very obvious that $T_{critical\text{-}two\ trail} > T_{statiscal}$, we accept the null hypothesis and there is no difference between the continuity equation method and Taylor's hypothesis method for influence at 95% confidence interval.

The continuity equation		Taylor's Hypothesis $U_{local\ velocity}$	
Mean	-0.121912844	Mean	-0.142857143
Standard Error	0.118309722	Standard Error	0.1458913
Standard Deviation	2.470379527	Standard Deviation	3.063717291
Sample Variance	6.102775008	Sample Variance	9.386363636
Kurtosis	416.3894897	Kurtosis	431.8204864
Skewness	-20.18181375	Skewness	-20.67850916
Range	55.173	Range	67
Minimum	-51	Minimum	-64
Maximum	4.173	Maximum	3
Sum	-53.154	Sum	-63
Count	436	Count	441

Table 4.2 Descriptive statistics of two $\partial U_x/\partial x$ results at $U_{local\ velocity}$ condition

F-Test Two-Sample for Variances	Continuity	Taylor's Hypothesis
Mean	-0.121912844	-0.14286
Variance	6.102775008	9.386364
Observations	436	441
df	9259	440
$F_{statistical}$	0.650174577	
P (F<= f) one-tail	3.72174E-06	
F Critical one-tail	0.854282867	

Table 4.3: F-Test: Two-Sample for variances at $U_{local\ velocity}$ condition

T-Test: Two-Sample Assuming Unequal Variances	Continuity	Taylor's Hypothesis
Mean	-0.121912844	-0.142857143
Variance	6.102775008	9.386363636
Observations	436	441
Hypothesized Mean Difference	0	
df	841	
T_{Stat}	0.111504538	
P (T<= t) one-tail	0.455621437	
t Critical one-tail	1.646667442	
P (T<= t) two-tail	0.911242873	
t Critical two-tail	1.962789611	

Table 4.4: T-Test: Two-Sample assuming unequal variances at $U_{local\ velocity}$ condition

4.8.2 Comparision Between Continuity and Taylor's Hypthesis Using $U_{\text{overal velocity}}$

To the comparision between continuity and Taylor's hypthesis using $U_{\text{overal velocity}}$, the statistical steps are repeated. The F-test is widely used for comparing different methods of variance. T-test is that of comparing whether there is difference between Continuity method and Taylor's hypthesis method by using $U_{\text{overal velocity}}$. Table 3.5 shows the statistical summary of two methods. In table 3.6, $F_{\text{statiscal}} < F_{\text{crirical-one tail}}$, thus two variances are not equal. In Table 3.7 comparing with Table 3.4, it is not obvious that $T_{\text{critical-two trail}} > T_{\text{calculated}}$. Although we still accept the null hypothesis and there is no difference between continuity method and Taylor's hypothesis method for influence at 95% confidence interval. But from the smaller difference between $T_{\text{critical-two trail}}$ and $T_{\text{calculated}}$, we can draw a conclusion that in Taylor's hypothesis, the $U_{\text{local velocity}}$ is more effective than $U_{\text{overall velocity}}$.

Continuity		Taylor's Hypothesis $U_{\text{overal velocity}}$	
Mean	-0.121912844	Mean	-0.248031496
Standard Error	0.118309722	Standard Error	0.253308198
Standard Deviation	2.470379527	Standard Deviation	4.037068368
Sample Variance	6.102775008	Sample Variance	16.29792101
Kurtosis	416.3894897	Kurtosis	248.6774922
Skewness	-20.18181375	Skewness	-15.6922022
Minimum	-51	Minimum	-64
Maximum	4.173	Maximum	3
Sum	-53.154	Sum	-63

Table 4.5 Descriptive statistics of two $\partial U_x/\partial x$ results at $U_{\text{overal velocity}}$ condition

F-Test Two-Sample for Variances	Continuity	Taylor's Hypothesis
Mean	-0.007164	-0.24706
Variance	0.50260154	16.234
Observations	250	255
df	9259	254
$F_{\text{statistical}}$	0.03095981	
P (F<= f) one-tail	0	
F Critical one-tail	0.81223517	

Table 4.6: F-Test: Two-Sample for variances at $U_{\text{overal velocity}}$ condition

T-Test: Two-Sample Assuming Unequal Variances	Continuity	Taylor's Hypothesis
Mean	-0.007164	-0.247058824
Variance	0.502601535	16.23399722
Observations	250	255
Hypothesized Mean Difference	0	
df	9259	
T_{Stat}	0.936110216	
P (T<= t) one-tail	0.175026481	
T Critical one-tail	1.650516879	
P (T<= t) two-tail	0.350052962	
$T_{\text{Critical two-tail}}$	1.268787728	

Table 4.7: T-Test: Two-Sample assuming unequal variances at $U_{\text{overal velocity}}$ condition

CHAPTER 5

RESULTS AND DISCUSSION

This chapter focuses mainly on the analysis of the experimental data and the uses of statistics to analyze the velocity measurement. There are two parts in this chapter, further statistical analysis and experimental conclusions.

After the experiment was accomplished, the individual frames of a sequence were analyzed using in-house software and Matlab^{TM} code. The final 11-frame average and over 2,000 frames average movies were composed. We had 18 sets of velocity data files and there were 2,000 images in each set. Those velocity data files contained the vector numbers, particle positions in the x, y, and z-axes, and vector value in x, y, and z directions. To obtain adequate statistical averages, Excel software was used for this. In order to determine the length of time needed for long-time statistics time period is needed. The analysis produced statistics report has information about mean, standard error (of the mean), standard deviation, variance, kurtosis, skewness, range, and confidence level. With this information, we can make decisions about our velocity files to determine how many vector numbers are needed to fully describe the flow.

5.1 Statistical Analysis of the Fluid Field

We used Excel to calculate the mean, standard deviation, skewness (how wide the curve is) and Kurtosis (how sharp the curve is) of each velocity data file on the x, y, and z directions. The four statistical factors and associated figures could tell us how many images are needed to describe the long-time average flow field.

Table 5.1 gives out the total vector number in each set.

Image Set #	1	2	3	4	5	6	7	8	9
Total Vector #	324,083	267,033	380,242	646,831	276,308	1302,551	544,235	1244,074	819,397
Image Set #	10	11	12	13	14	15	16	17	18
Total Vector #	766,613	407,005	904,909	703,154	668,182	924,582	884,148	713,027	1161,697

Table 5.1: Total vector number in each data set

Note that in each set of image numbers, the total vector numbers are different. Thus, the total vector number needs to be determined rather than the number of image sets. Sets 12 and 18 are the best two sets because set 12 has the highest seeding density, which is 651 vectors/image. Set 18 has 2,300 frames compared to the 2,000 images of the other sets.

Based on the statistical analysis of the accumulate vector number in Table 5.2, 5.3, 5.4, and 5.5 and by using 1 standard deviation (the standard deviation is a measure of how widely values are dispersed from the average value) in Fig. 5.1, 5.2, 5.3, and 5.4, we can display Y-error bars at each data point. By looking up the plots manually, we can estimate how many vector numbers are needed to describe the flow field.

Set Number	**Accumulate Vector Number**	**U (x)**			
		Mean	**Standard Deviation**	**Skewness**	**Kurtosis**
1	324,083	-1.40369	12.32525914	-1.32424588	17.798008
2	591,116	-0.74964	11.523989	-0.98646679	7.6578623
3	971,358	-0.64159	11.50643213	-0.71731229	5.0341212
4	1,618,189	-0.34045	10.97177404	-0.58798172	4.2713512
5	1,894,497	-0.41664	11.19663539	-0.65987994	4.2530551
6	3,197,048	0.71358	11.49492858	-0.27639673	2.4762692
7	3,741,283	0.833959	11.55619408	-0.17192045	2.5103267
8	4,985,357	1.545951	12.67802938	0.263395449	1.6665929
9	5,804,754	1.611149	12.87512166	0.393104267	1.7319876
10	6,571,367	0.647743	12.5496296	0.538546156	2.0362846
11	6,978,372	1.62073	12.71492218	0.475327577	2.0626657
12	7,883,281	0.8404	12.59998053	0.615301545	2.449516
13	8,586,435	0.8404	12.59998053	0.615301545	2.449516
14	9,254,617	1.653239	12.77903984	0.538563614	2.4252023
15	10,179,199	0.982023	12.39831567	0.631630353	2.6940506
16	11,063,347	1.718228	12.64916677	0.625186521	2.6331732
17	11,776,374	1.139817	12.39457113	0.717978986	2.8870058
18	12,938,071	1.744193	12.3778614	0.666024061	2.7844706

Table 5.2: X-direction velocity values in each data set

Set Number	**Accumulate Vector Number**	**U (y)**			
		Mean	**Standard Deviation**	**Skewness**	**Kurtosis**
1	324,083	2.392822	27.38988492	1.105534937	15.412745
2	591,116	1.006398	25.79495042	0.397641025	13.4473295
3	971,358	0.285799	25.3088241	0.238083728	14.5644103
4	1,618,189	-0.03778	24.42622377	0.118558636	12.3442184
5	1,894,497	-0.23251	24.46834128	-0.00180171	12.034502
6	3,197,048	-0.37896	24.20625337	-0.07762671	9.93514512
7	3,741,283	-0.41774	24.00240418	-0.19610677	10.2147369
8	4,985,357	-0.30807	24.41245385	-0.16473673	8.56101062
9	5,804,754	-0.2995	24.39190931	-0.16607111	8.42894985
10	6,571,367	-0.2562	23.91539134	-0.06219021	8.22843587
11	6,978,372	-0.3096	23.87947075	-0.10013398	8.37232209
12	7,883,281	-0.33092	23.89694928	-0.11464773	8.47690912
13	8,586,435	-0.33092	23.89694928	-0.11464773	8.47690912
14	9,254,617	-0.33036	23.85575754	-0.0991794	8.6117081
15	10,179,199	-0.33053	23.66970524	-0.1104659	8.58603139
16	11,063,347	-0.30212	23.59952409	-0.08959869	8.59640365
17	11,776,374	-0.2214	23.46217796	-0.06122607	8.49902582
18	12,938,071	-0.1703	23.30297392	-0.04131184	8.54428049

Table 5.3: Y-direction velocity values in each data set

Set Number	**Accumulate Vector Number**	**U (z)**			
		Mean	**Standard Deviation**	**Skewness**	**Kurtosis**
1	324,083	9.616116	12.16240244	0.7134486	-0.26612
2	591,116	9.175067	10.93186	0.7316941	-0.48968
3	971,358	9.514482	11.4782543	0.7823507	-0.52214
4	1,618,189	9.419402	11.57795631	0.7871234	-0.55493
5	1,894,497	9.433893	11.97800871	0.8099862	-0.45297
6	3,197,048	8.633014	10.78714978	0.7767474	-0.54041
7	3,741,283	8.712008	10.87851427	0.7985136	-0.49519
8	4,985,357	8.273858	10.28606928	0.7914423	-0.51185
9	5,804,754	8.18503	10.41967789	0.7653855	-0.5448
10	6,571,367	8.069365	10.24383609	0.7715948	-0.53722
11	6,978,372	7.249179	10.47164142	0.7667834	-0.49271
12	7,883,281	8.157945	10.29006472	0.7748507	-0.52538
13	8,586,435	8.157945	10.29006472	0.7748507	-0.52538
14	9,254,617	7.397129	10.45437987	0.7942831	-0.41062
15	10,179,199	8.092712	10.18377819	0.7973047	-0.47707
16	11,063,347	7.294496	10.28103178	0.8065667	-0.39254
17	11,776,374	7.92299	10.11183758	0.7986835	-0.42386
18	12,938,071	7.310612	10.18646284	0.8084773	-0.36123

Table 5.4: Z-direction velocity values in each data set

Set Number	**Accumulate Vector Number**	$\lvert U\rvert = (Ux^{\wedge}2+Uy^{\wedge}2+Uz^{\wedge}2)^{\wedge}0.5$			
		Mean	**Standard Deviation**	**Skewness**	**Kurtosis**
1	324,083	10.00828	32.40434912	1.8667735	23.54554
2	591,116	9.260489	30.29335493	1.290973	15.48268
3	971,358	9.540371	30.07797998	1.0877929	15.41872
4	1,618,189	9.425628	29.17309215	0.9896171	13.0741
5	1,894,497	9.445951	29.4539821	1.0447595	12.77196
6	3,197,048	8.67074	28.88665238	0.8281048	10.25334
7	3,741,283	8.761797	28.77504302	0.8400229	10.53033
8	4,985,357	8.422683	29.3684108	0.850233	8.736729
9	5,804,754	8.347468	29.4839564	0.8763136	8.622284
10	6,571,367	8.099374	28.88555563	0.9430048	8.493657
11	6,978,372	7.434595	29.009544	0.9077004	8.636731
12	7,883,281	8.207792	28.90863411	0.9960591	8.839352
13	8,586,435	8.207792	28.90863411	0.9960591	8.839352
14	9,254,617	7.586821	29.01198176	0.9647658	8.9561
15	10,179,199	8.158775	28.59514847	1.023159	9.011406
16	11,063,347	7.500217	28.68167658	1.0244198	8.999213
17	11,776,374	8.00762	28.39627524	1.0757034	8.985984
18	12,938,071	7.51773	28.28434322	1.0482987	8.993803

Table 5.5: Velocity values in each data set

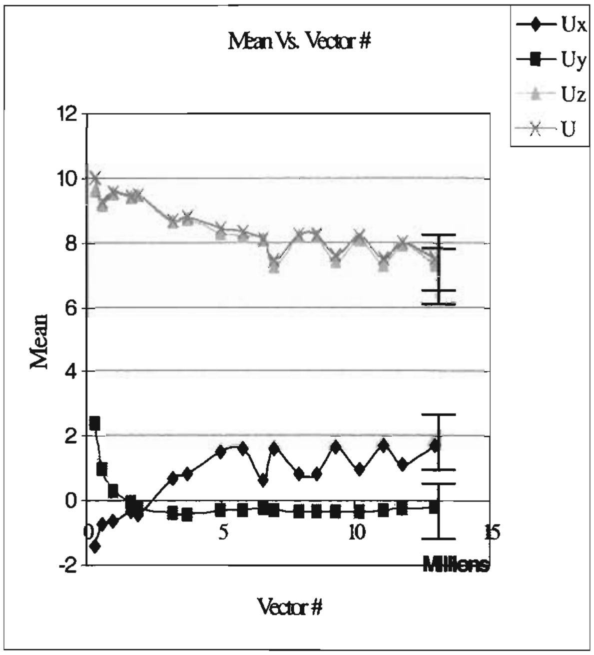

Figure 5.1: X, Y, Z direction mean vs. vector numbers

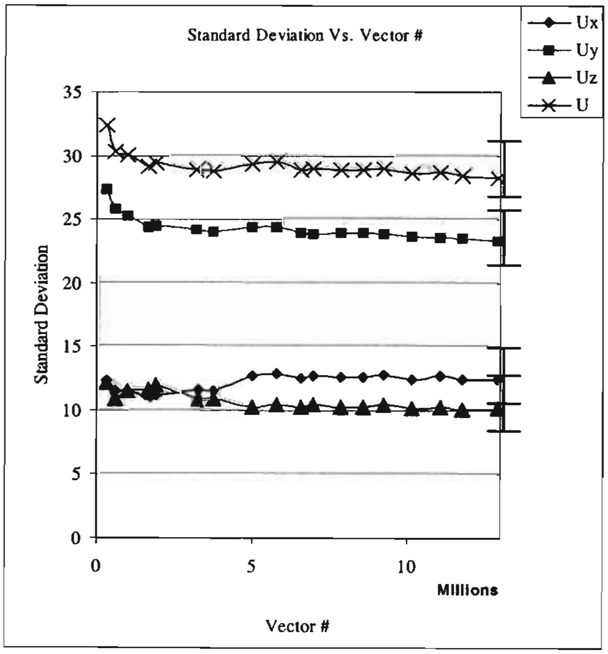

Figure 5.2: X, Y, Z direction standard deviation vs. vector numbers

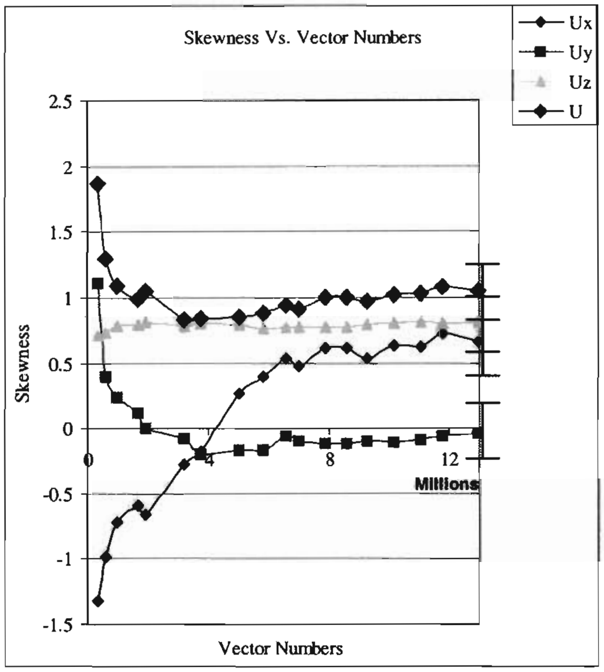

Figure 5.3: X, Y, Z direction skewness vs. vector numbers

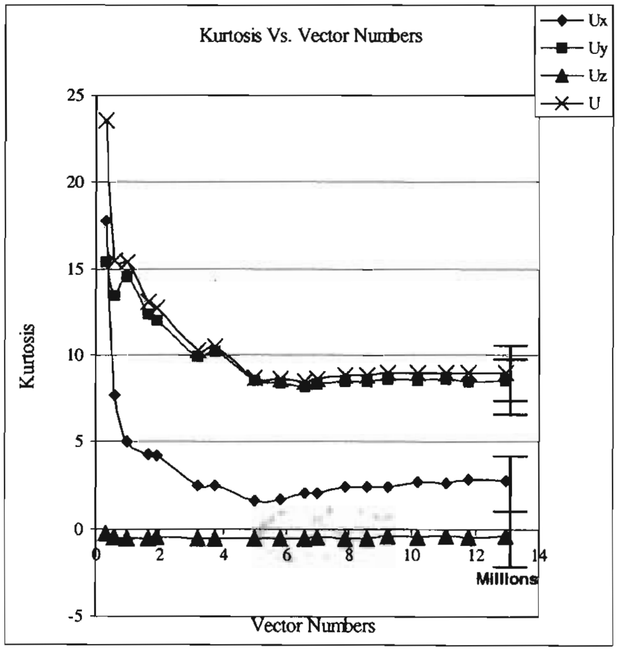

Figure 5.4: X, Y, Z direction kurtosis vs. vector numbers

Table 5.6 is the vector number estimate in each direction for the different statistical factors. From Table 5.6, we can see that, to satisfy all of the statistical factors, we probably need about 3.2×10^6 vectors in each image.

Standard Deviation	U_x Vector # ($\times10^6$)	U_y Vector # ($\times10^6$)	U_z Vector # ($\times10^6$)	U Vector # ($\times10^6$)
Average	3.197	0.971	3.197	3.197
Standard Dev.	3.197	1.64	3.197	1.64
Skewness	0.971	0.591	1.894	0.971
Kurtosis	0.591	1.64	0.591	1.64

Table 5.6: Vector number needed in each velocity direction at different statistical factors

5.2 Determination of Average Number of Frames to Obtain a Reasonable Statistical Average

The pictures of the flow patterns and chemical species distributions were recorded for each time step (11-frame average) or 0.3667 second. In the visuals, 33 frames or 1.1 second of computational information are shown. The experimental results are a moving window average over 11-frame (0.3667 second period). Each subsequent frame in the sequence is the same average shifted by one frame forward. This creates the moving window average.

In order to obtain a statically smooth representative but still dynamic in nature, the number of vectors in each representative frame had to be established. This was done by changing the window average from 7 to 15 and viewing the short sequences to see which window average sequence appeared smooth and still maintained the physics of the event observed.

The 11-frame average movie captured the flow structures clearly and at the same time provided a smooth sequence to view. To make sure the 11-frame average movie was adequate to reflect the motions, the 13-frame and 15-frame average sequences were used for comparison. In the 13-frame and 15-frame average sequences results, there was not a big difference when compared to the 11-frame average sequences results. Thus, the 11-frame average sequences represented the best minimum number of images to reflect the quantitative characterization of the mixing processes.

Short sequences were studied. The first is images number 24-36 in set 18, which had a vortex on the upper left of the mixer. The second is images number 99-129, which clearly showed two jets quickly met at the center of the mixer and flowed to the outlet edge. The third part is image number 161-180, which showed the two jets flowed from the two inlet tubes and waving up and down. This flapping is a consequence of jet interactions and jet instability at higher Reynolds numbers.

5.3 Graphical Analysis for the Average Fluid Field and Instantaneous Fluid Field

We would like to use color representations, but this is not possible due to the limitation imposed by the printed page. Thus in this paper the figures are in grayscale levels and are not moving. However, the same figures, in full color, can be found at the URL [http://www.che.eng.ohio-state.edu/~brodkey/APS-DFD-01/].

5.3.1 Graphical Analysis for the Average Flow Field

A long-time, average 3-D velocity results are shown. The Reynolds number is 2,000 based on the inlet pipe diameter of 0.019m and the average inlet velocity. The reason for using the long-time average images are, first, they can tell us the globe characters about the globe characters about the mixing procedure. Second, they are a critical measure of comparison with computational results. If there do not check well then dynamic comparisons are bound to fail.

The three views in Fig. 5.5 are two-dimensional orthogonal slices between the two jets one of 21 in each case. Velocity vectors on the horizontal plane (a) are given. The image (b) is the central vertical plane in the jet direction. The image (c) is the central plane orthogonal to the other two planes. The three-dimensional cuts can be scanned across the geometry to provide spatial 2,000-frame average pictures of the flow field were shown in the URL.

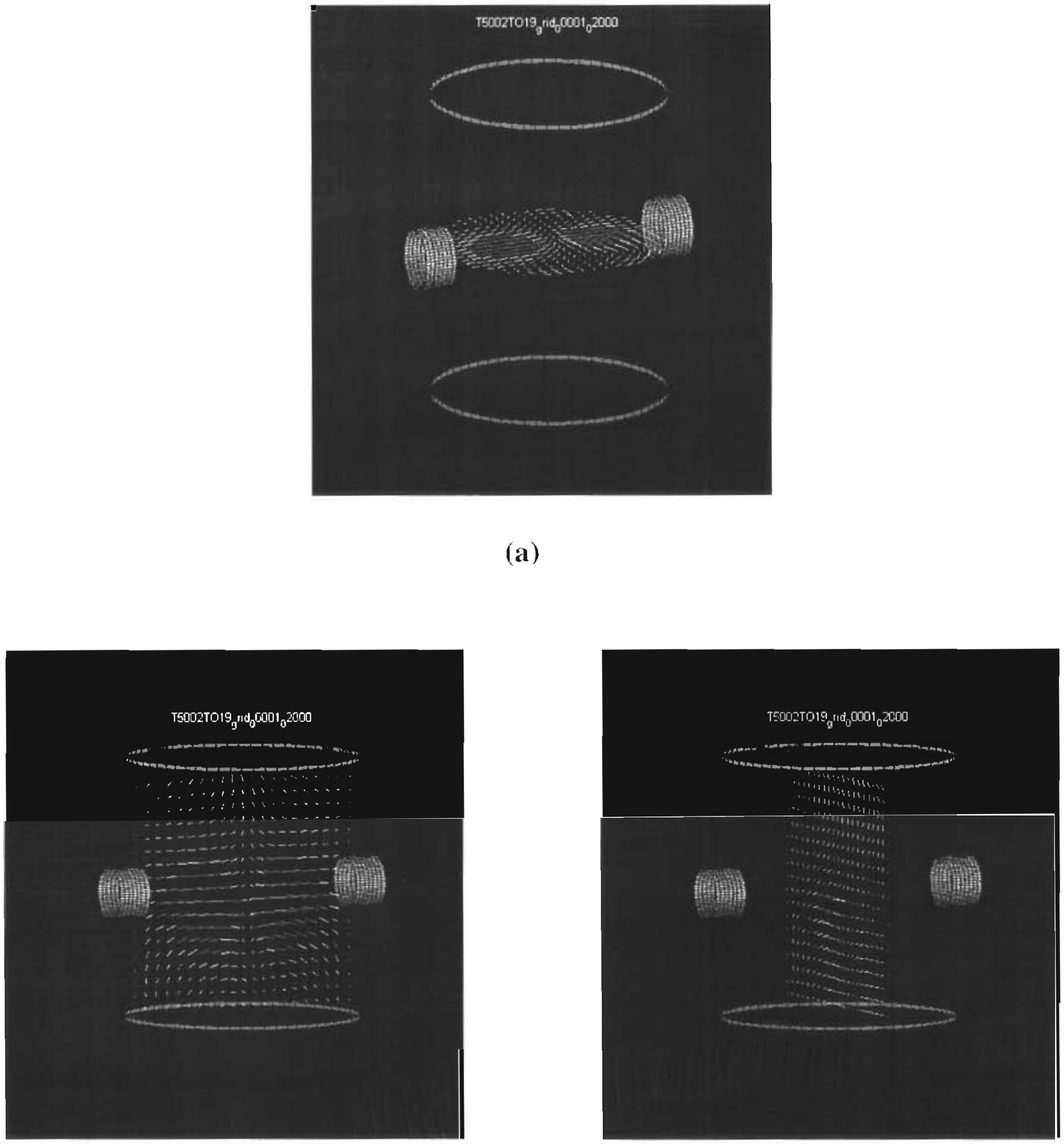

(a)

(b)

(c)

Fig. 5.5 3-D, time-averaged, velocity vectors in the horizontal (xy) plane (a), the jet (yz) plane (b), and the lateral (xz) plane (c). The velocity vectors shown here are the actual vectors on the 21^2 grids

The long-time averaged velocity field, shown in Fig. 5.6, looks regular with very little interaction or mixing at the region where the two jets collide. The view does not show the single outlet that is at the top of the vessel. The reason for using long-time average images is because that they can illustrate the globe characters about the flow field and are a critical measure of comparison with computational results. The dividing velocity surfaces between the jets are clearly visible. With software available, the three-dimensional view can be rotated and a film clip can be made of the rotation in space. However, doing much else with the representation shown in Fig. 5.6 is difficult. It is just simply too complex for ease of interpretation.

We previously found that scanning velocity planes can give a better picture of the flow field. Fig. 5.7 provides an idea for the averaged results; only five slices of the 21 velocity vectors are shown in Fig. 5.7. Normally (in the URL), we do this as a loop, so that a moving picture can visualize the 3-D field in our minds. The rest selection was to use color examples of our results that have been brought together on our URL [http://www.che.eng.ohio-state.edu/~brodkey/APS-DFD-01/]. In the posted material, we used both color and muli-scanning representational views.

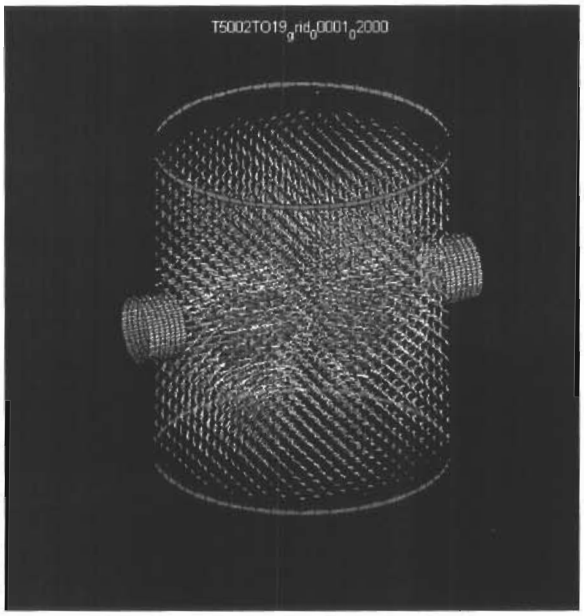

Fig. 5.6 Long-time averaged velocity field at a jet Reynolds number of 2,000.

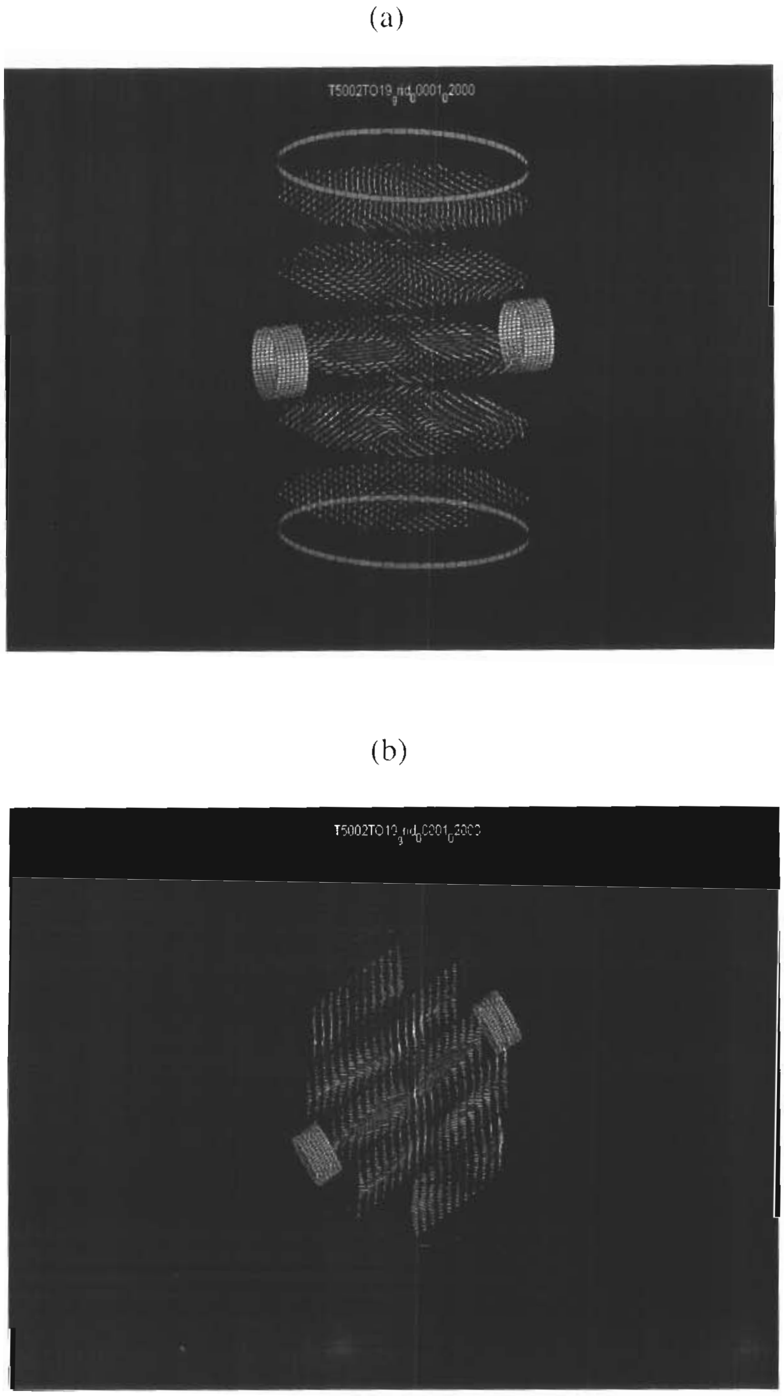

Fig. 5.7 Long-time, average 3-D velocity fields of front (a) and top views (b) at a jet Reynolds number of 2,000. (Five Planes of 21^3)

5.3.2 Graphical Analysis for the Instantaneous Fluid Field

Often long-time averaged results are not an adequate database for important problems that depend more on the 11-frame average results of the flow more than the statistical average characteristics. For example, problems that involve chemical reactions and associated selectivity to final products are sensitive to the localized characteristics of the flow. When two components react, they react on a molecular basis, not on the average. Although mixing flow fields are the hardest to represent on the static pages, Fig. 5.8 and Fig. 5.9 reflect an attempt to show a bit of the mixing nature of the flow. Some results such as these have been made as animations and presented on our web site. The jets meet at the center of the mixer and form a pancake flow. The pancake flow's direction oscillates. The unsteady vortexes presented in the vessel are unsymmetrical in locations and intensities. Each subsequent frame in this sequence is the 11-frame average shifted by one frame forward.

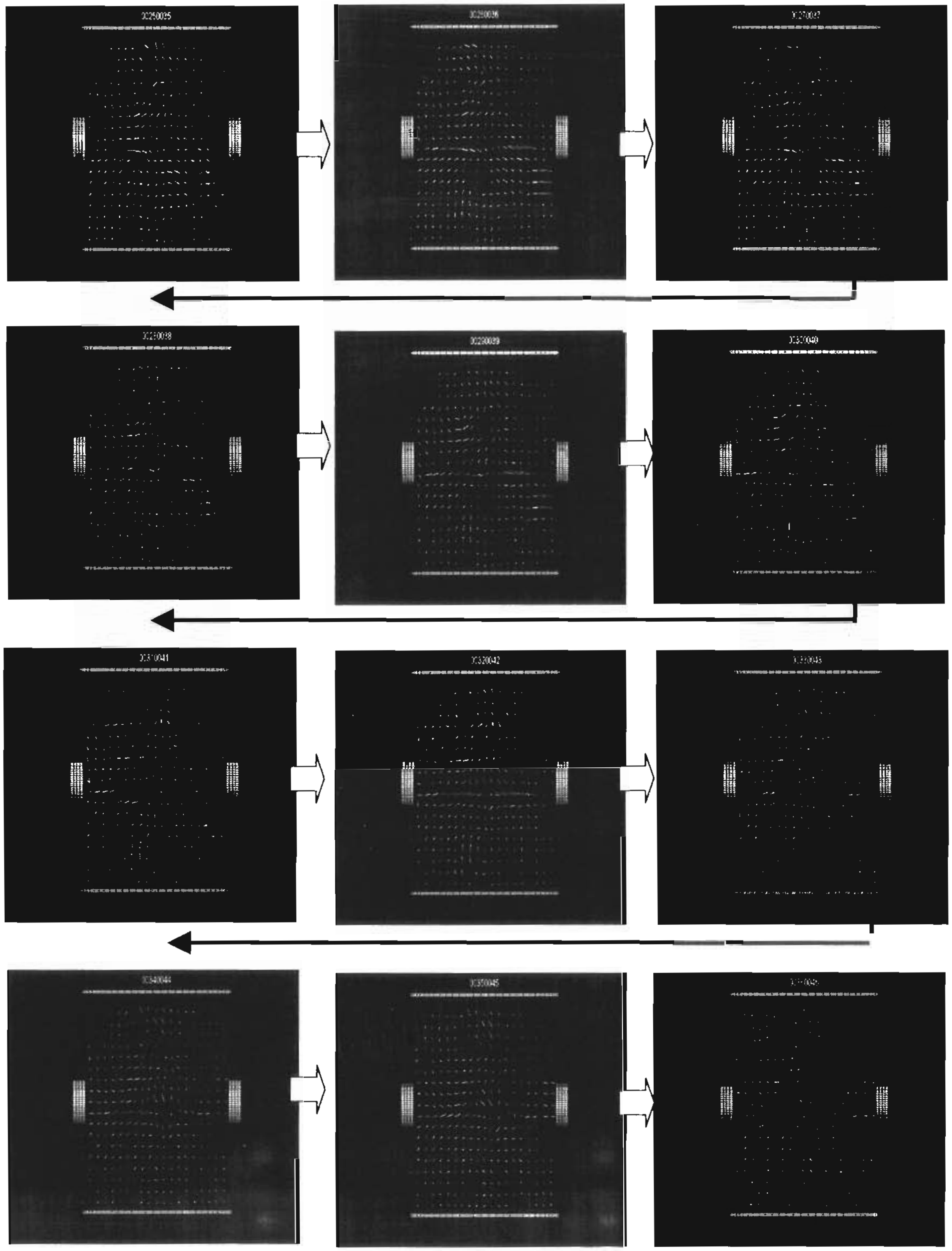

Fig. 5.8 11-frame average results of the front view flow for 11-frame averages at a jet Reynolds number of 2,000.

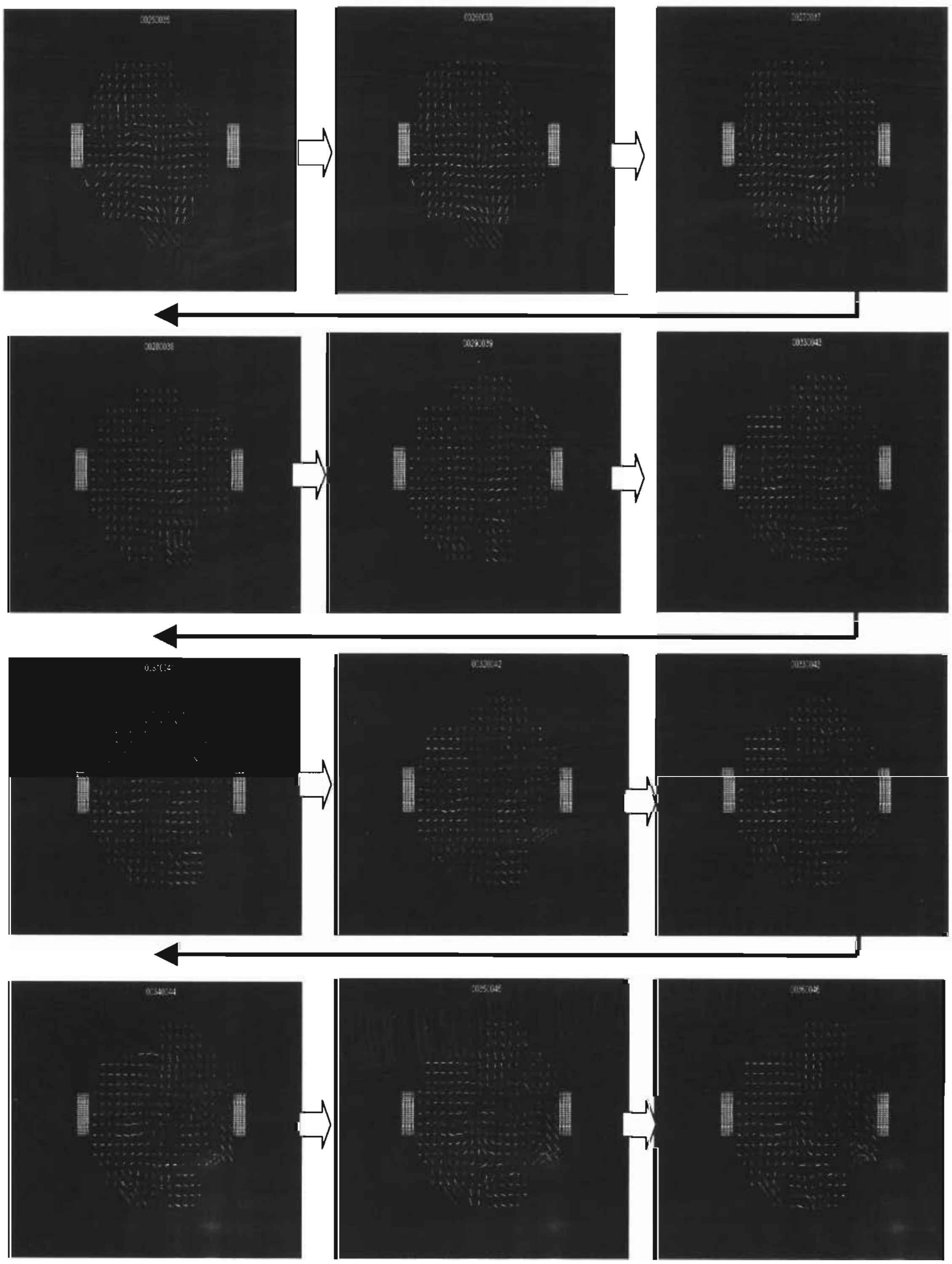

Fig. 5.9 11-frame average results of the top flow for 11-frame averages at a jet Reynolds number of 2,000.

CHAPTER 6

CONCLUSIONS AND RECOMMENDATIONS

PTV is an excellent tool for visualizing the flow patterns for the two opposed jets mixer. The long-time average and instantaneous sequences of frames movies are examined.

6.1 Conclusions

The following conclusions have been drawn:

1. The study of the opposed-jet configuration involved a time-resolved, full-field, systematic examination of the three-dimensional flow.
2. The characteristics of the flow near the interface are consistent with the expected three-dimensional picture for all three planes.
3. The opposed jet mixer generates large scale, three-dimensional, unsteady motions at a jet Reynolds number of 2,000.
4. The jets meet at the center of the vessel and form a complex secondary pancake flow. The pancake sheet expands in all directions. The pancake flow is unsteady

and its direction oscillates. Parts of the secondary pancake flow in the horizontal directions meet the wall and bottom of the vessel and become wall flows. Four vortices often form.

5. Two-dimensional representations even in color do not allow adequate representations of the resulting velocity and dependent parameter fields. More complex and dynamic representation must be used to descripe the flow field. Microsoft ™ PowerPoint and internet animated images can be used to overcome this limitation.
6. The high Reynolds number flows are found to have the basic flow patterns found in the previous low Reynolds number flows, although the flows are turbulent.
7. Both continuity equation and Taylor's hypothesis were successfully used to find the $\partial U_x/\partial x$ term in the experimental data analysis.
8. In Taylor's hypothesis, $U_{\text{local velocity}}$ is more effective than $U_{\text{overall velocity}}$ which means the velocity on each point fits the Taylor's hypothesis.

6.2 Recommendations

6.2.1 Camera Spatial Resolution Recommendation

For our current research using CCD cameras, a resolution of 640H×480V pixels was used and seemed to be adequate for the acquisition of processing of particle images for 3-D PTV. However, a finer spatial resolution would obviously be better in resolving finer velocity motions. This would also allow using smaller size particles. Better illumination systems are a needed factor to compensate for the possible contrast loss with smaller particles. Increasing spatial resolution of the cameras could potentially allow the successful imaging of several thousand particles. This would allow resolving finer structures of the flow on the average.

6.2.2 Cameras Arrange Recommendation

In order to determine the flow field characteristics in our project, it is highly desirable to obtain higher yields of velocity vectors either through an enhanced spatial resolution of the imaging system or through other algorithmic approaches. Since the 3-D volume imaging onto a 2-D plane limits the seeding density of the tracer particles in the flow field, the 3-D PTV has generic limitations of the yield of 3-D velocity data density. However, this yield could be enhanced if a third or fourth camera was used in a configuration such as the one shown in Figure 6.1. Others have done this. The third camera would provide redundancy in the 3-D velocity extraction process and would significantly reduce the particle-crowding problem. The number of vectors for each realization could reach several thousand per frame.

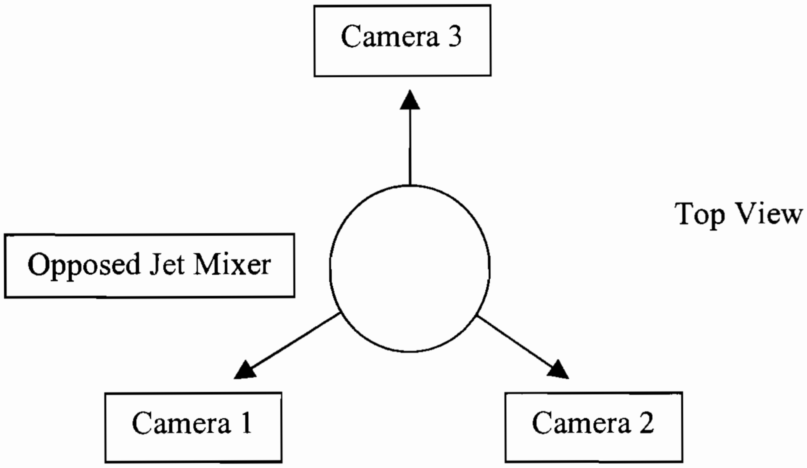

Fig 6.1: Recommendation configuration of the three-camera system

6.3 Particle Path Investigations Recommendation

Particle paths that are generated from the experimental velocity vector field can be averaged in space and time and connected to develop a series of streak lines. Equations can then be used in a simulation program to easily determine the response of the flow to various time-dependent inlet conditions.

BIBLIOGRAPHY

[1] Atkinson, K. N., Z. A. Khan, and J. H. Whitelaw, "Experimental Investigation of Opposed Jets Discharging Normally into a Cross-Stream", J. Fluid Mech., Volume: **115**, 493-504 (1982).

[2] Cooper, D., D. C. Jackson, B. E. Launder, and G. X. Liao, "Impinging Jet studies for Turbulence Model Assessment-I. Flow-Field Experiments", Int. J. Heat & Mass Trans., Volume: **36**, 2675-2684 (1993).

[3] Yang Zhao, R. S. Brodkey, D. Unger, F.J. Muzzio, "Jet Mixing, Comparison of CFD with Full-field, Velocity Vector Measurements: Non-time Dependent Case", http://www.er6.eng.ohio-state.edu/~brodkey/ojindex.htm. See item on the 5th Chemical Congress of North America, Cancun, Quintana Roo, Mexico, (1997).

[4] Craft, T. J., L. J. W. Graham, and B. E. Launder, "New Wall-Reflection Model Applied to the Turbulent Impinging Jet", AIAA Journal, Volume: **30**, 2970-2972 (1992).

[5] Cushman, John H and Moroni, Monica, "Statistical Mechanics with three-dimensional Particle Tracking Velocimetry Experiments in the Study of Anomalous Dispersion", Part I, Physics of Fluids, Volume: 13, Issue: 1, 75-80, (2001).

[6] S. J. Haam, R.S. Brodkey, I. Ford, L. Klaboch, M. Placnik, and V. Vanecek, "Laser Doppler Anemometry Measurements in an Index of Refraction Matched Column in the Presence of Dispersed Beads" Part I, International Journal of Multi-Phase Flow, Volume: **26,** Issue 9, 1419-1438 (2000).

[7] S. J. Haam, and R.S. Brodkey, "Motions of Dispersed Beads Obtained by Particle Tracking Velocimetry Measurements" Part II, International Journal of Multiphase Flow, Volume: **26,** Issue 9, 1438-1451 (2000).

[8] Jian Sheng, Hui Meng, and Rodney O. Fox, "Validation of CFD Simulation of a Stirred Tank Using Particle Image Velocimetry Data", The Canadian Journal of Chem. Eng., Volume: **76**, 511-525 (1998).

[9] Ander Bankker, Ahmad H. Haidari, and Lanre M. Oshinowo, "Realize Greater Benefits from CFD", CEP, Volume: **32**, 45-53 (2001).

[10] McComb, D., "Large Eddy Simulation of Complex Engineering and Geophysical Flows", Flow Measurement and Instrumentation, Volume: **7**, Issue: 1, 57-58 (1996).

[11] Yang Zhao, and R. S. Brodkey, "Particle Paths in Three-dimensional Flow Fields as A Means of Study: Opposing Jet mixing System", Power Technology, Volume: **100,** 161-165 (1998).

[12] Poinsot, T. "Application of Direct Numerical Simulation to Premixer Turbulent Combustion", Fuel and Energy Abstracts, Volume: 37, Issue: 4, 285-294, (1996).

[13] Wood, P., A. Hrymak, R. Yeo, D. Johnson, and A. Tygi, "Experimental and Computational Studies of the Fluid Mechanics in an Opposed Jet Mixing Head", Physics of Fluids A, Volume: **3**, 1362 (1991).

[14] W.D. McComb, "The Physics of Fluid Turbulence", Oxford University Press, Oxford, New York, (1990).

[15] R. S. Brodkey, "The Phenomena of Fluid Motions", Dover Publications, Inc. Mineola, New York, (1986).

[16] Lee, L. J., J. M. Ottino, W. E. Ranz, and C. W. Macosko, "Impingement Mixing in Reaction Injection Molding", Poly. Eng. Sci., Volume: **20**, 868-874 (1980).

[17] Tucker, C. L., and N. P. Suh, "Mixing for Reaction Injection Molding em Dash 1. Impingement", Polymer. Mixing of Liquids, Poly. Eng. Sci., Volume: **20**, 875-866 (1980).

[18] Kolodziej, P, C. W. Macosko, and W. E. Ranz "The Influence of Impingement Mixing on Striation Thickness Distribution and Properties in Fast Polyurethane Polymerization", Poly. Eng. Sic., Volume: **22**, 388-392 (1982).

[19] Ogawa, N., and H. Maki, "Studies on Turbulent Opposed Turbulent Jets. (Impact Position and Turbulent Component in Jet Center)", JSME International Journal, Series 2: Fluids Engineering, Heat Transfer, Power, Combustion, Thermo physical Properties., Volume: **35**, 205-211 (1992).

[20] Wood, P., A. Hrymak, R. Yeo, D. Johnson, and A. Tygi, "Experimental and Computational Studies of the Fluid Mechanics in an Opposed Jet Mixing Head", Physics of Fluids A, Volume: **3**, 1362-1372 (1991).

[21] Johnson, D.A., P.E. Wood, and A. N. Hrymak "The Effect of Geometrical Parameters on the Flow Field of an Opposed Jet RIM Mix Head: Equal Flow and Matched Fluids", Can. J. Chem. Eng., Volume: **74**, 40-48 (1996).

[22] - [25] Lee, L. J., J. M. Ottino, W. E. Ranz, and C. W. Macosko, "Impingement Mixing in Reaction Injection Molding", Poly. Eng. Sci., Volume: **20**, 868-874 (1980).

[26] Malguaranera, and N. P. Suh, "A Swirling Round Turbulent Jet: Mean-Flow Measurements", Journal of Applied Mechanics, Volume: 4, 615-625 (1962).

[27] - [29] Yang Zhao, and Robert S. Brodkey, "Averaged and time-resolved, Full-Field (Three-Dimensional), Measurement of Unsteady Opposed Jets", The Canadian Journal of Chem. Eng., Volume: **76**, 536-545 (1998).

[30] Yang Zhao, R.S. Brodkey, and S. Nakamura, "Study of 3-D Mixing Processes by Numerical and Experimental Approaches", ASME Fluids Engineering Summer Conference. Boston, Massachusetts, (2001).

[31] R.S. Brodkey, D.R. Unger, and F.J.Muzzio. "Experimental and Numerical Characterization of Viscous Flow and Mixing in an Impinging Jet Contactor", Can. J. Chem. Eng., Volume: **76**, 546-555 (1998).

[32] Bruun, H., "Hot Wire Data Corrections in Low and High Turbulence Intensity Flows", Journal of Physics E: Scientific Instruments, Volume: **5**, Issue: 8, 812-818 (1972).

[33] Gauezennec YG, and Kiritsis N "Statistical Investigation of Errors in Particle Image Velocimetry", Exp. Fluids, Volume: **10**, 138-146 (1990).

[34] Forder, P. W., "A Novel Approach to Laser Doppler Velocimetry and Anemometry", Journal of Physics E: Scientific Instruments, Volume: **14**, Issue: 8, 1014-1018, (1981).

[35] Y. Guezennec, R.S. Brodkey, N. Trigui, and J.C. Kent, "Algorithms for Full Automated Three-dimensional Particle Tracking Velocimetry", Experiments in Fluids, Volume: **17**, 209-219, (1994).

[36] Cowen, E. A. Monismith, S. G., Cowen, E., and A. Monismith, S. G. "A Hybrid Digital Particle Tracking Velocimetry Technique", Experiments in Fluids, Volume: **22**, Issue: 3, 199-211 (1997).

[37] Harry C. Hershey, Jacques L. Zakin, and Robert Simha "Numerical Differentiation of Equally Spaced and Not Equally Spaced Experimental Data ", Ind. and Eng. Chem. Fundamentals, Volume: **6,** No.3, 313-321 (1967).

APPENDIX

EXPERIMENAL EQUIPMENTS AND COMPUTER CODES

Equipment:

PULNiX TM-6701AN Progressive Scanning Full Frame Shutter Camera

Product No. PD-1212 AR-D

PULNiX America Inc.

1330 Orleans Drive

Sunnyvale, CA 94089

Dwyer Rotameters

± 1 gph

Pump 1&2:

Flotec, Inc.

Model 360

Norwalk, CA 90650

115 volts/ 5A CMP / 1.5 amps / 60 Hz

Water Tank

Sterilite™ 45 Gal./170 L

Townsend MA 01469

Lighting:

10,000 Volts Strobex Lamp

Chadwick Helmuth

Model: 279D

Part No. 973-9390A

Serial 1174

VEXTA Stepping Motor

2-Phase 1.80 DEG/ STEP

Model PH268-E2.3

Oriental Motor Co. LTD

Dying

Pylakrome Oil Flour Yellow LX 8248

Pylam Products Company, Inc

1001 Stewart Ave

Garden City, NY 11530

Particles:

Microcarrier Beads

SoloHill Engineering, Inc

Model No. P102 90150

150 um Density: 1.04

4220 Varsity Drive

Ann Arbor, MI 48108

Gateway

System: Microsoft Windows 98

Pentium III Processor

128.0 MB RAM

12.6G

Point Number	t (h=1/60)	t	f(t)	f_n	**dY(0)**
1	1	1	3	f_{-3}	3.5142857
2	1+1/60	1.016667	3.8	f_{-2}	**dY(0)/dt**
3	1+2/60	1.033333	4.6	f_{-1}	-10.571428
4	1+3/60	1.05	5.4	f_0	
5	1+4/60	1.066667	4.3	f_1	
6	1+5/60	1.083333	3.2	f_2	
7	1+6/60	1.1	2.4	f_3	

Smoothing:

$$Y_0 = \frac{1}{21}(-2f_{-3} + 3f_{-2} + 6f_{-1} + 7f_0 + 6f_1 + 3f_2 - 2f_3)$$

Sloping:

$$\frac{dY_0}{dt} = \frac{1}{252 \times \frac{1}{60}}(22f_{-3} - 67f_{-2} - 58f_{-1} + 0f_0 + 58f_1 + 67f_2 - 22f_3)$$

Plug in the t and f (t) values we have:

Y_0=3.5142857
dY_0/dt=-10.571428

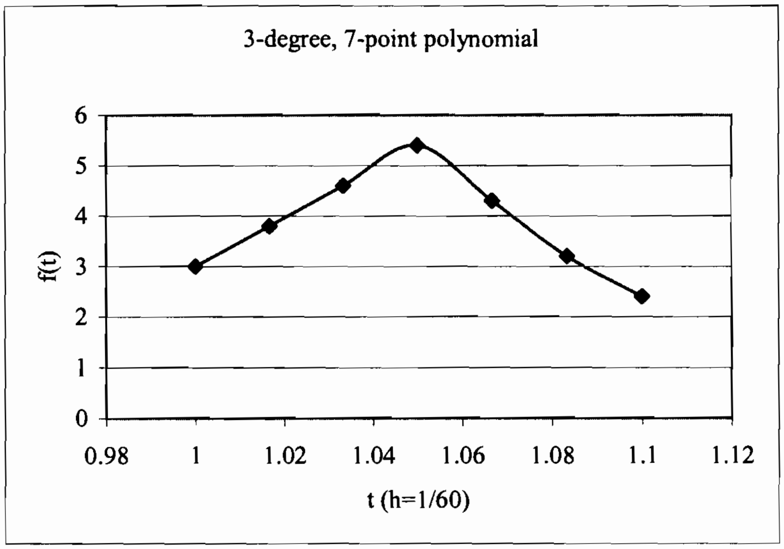

Point Number	t (h=1/60)	t	f(t)	f_n	**Y(0)**
1	1	1	3.3	f_{-3}	3.157143
2	1+1/60	1.016667	3.7	f_{-2}	**dY(0)/dt**
3	1+2/60	1.033333	3.4	f_{-1}	-7.547619
4	1+3/60	1.05	3.6	f_0	
5	1+4/60	1.066667	3.2	f_1	
6	1+5/60	1.083333	3.4	f_2	
7	1+6/60	1.1	3.3	f_3	

Smoothing:

$$Y_0 = \frac{1}{21}(-2f_{-3} + 3f_{-2} + 6f_{-1} + 7f_0 + 6f_1 + 3f_2 - 2f_3)$$

Sloping:

$$\frac{dY_0}{dt} = \frac{1}{252 \times \frac{1}{60}}(22f_{-3} - 67f_{-2} - 58f_{-1} + 0f_0 + 58f_1 + 67f_2 - 22f_3)$$

Plug in the t and f (t) values we have:

Y_0=3.157143

dY_0/dt=-7.547619

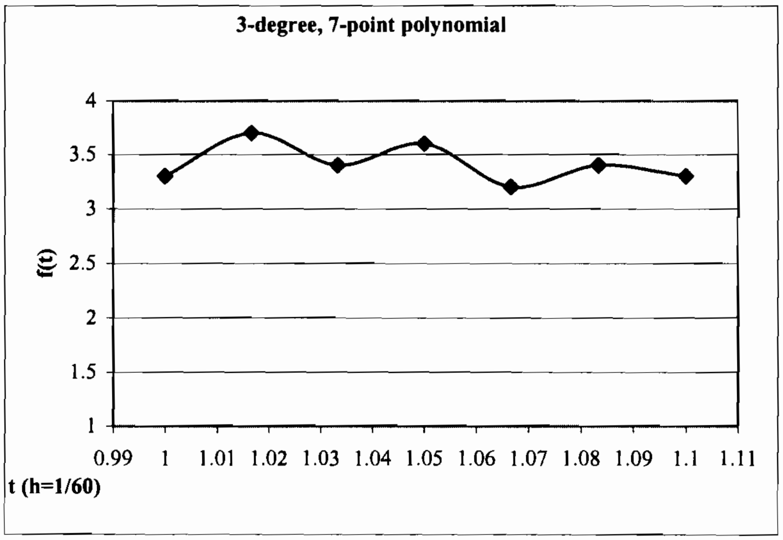

N'	S	D	C	C	C	C	C	C	C
	-2	70	...	69	4	-6	4	-1	...
	-1	35	...	2	27	12	-8	2	...
5	0	35	...	-3	12	17	12	-3	...
	1	35	...	2	-8	12	27	2	...
	-3	42	39	8	-4	-4	1	4	-2
	-2	42	8	19	16	6	-4	-7	4
	-1	42	-4	16	19	12	2	-4	1
7	0	21	-2	3	6	7	6	3	-2

Table 15: Orthogonal least squares coefficients for third-degree smoothing formulas

Taken from Hershey et al. (1967)

N'	m	S	D	C	C	C	C	C	C	C	C	C
5		-2	70	...	...	-54	13	40	27	-26	...	...
		-1	70	...	...	-34	3	20	17	-6	...	...
		0	10	...	...	-2	-1	0	1	2	...	...
7		1	70	...	...	6	-17	-20	-3	34	...	...
		-3	84	...	-39	-6	15	24	21	6	-21	...
		-2	84	...	-29	-6	93	16	15	6	-11	...
		-1	84	...	-19	-6	-1	8	9	6	-1	...
		0	28	...	-3	-2	603	0	1	2	3	...
9		-4	4620	-1428	-511	166	433	800	757	474	-49	-812
		-3	4620	-1148	-441	86	263	600	587	394	21	-532
		-2	4620	-868	-371	6	93	400	417	314	91	-252
		-1	4620	-588	-301	-74	-1	200	247	234	161	28
		0	60	-4	-3	-2		0	1	2	3	4
7		-3	252	...	-257	122	185	72	-77	-122	27	...
		-2	252	...	-122	17	62	48	10	-17	2	...
		-1	252	...	-29	-46	-19	24	55	46	-31	...
		0	252	...	22	-67	-58	0	58	67	-22	...

Table 16: Orthogonal least squares coefficients for sloping formulas

Taken from Hershey et al. (1967)

```
%   continuity.m  for calculation by using continuity equation.
%   This program calculates the velocity directive by using continuity
equation.
%   Dong Zhang 11/15/2001
load test.dat; %Load 11-point average grid files; in order to be convenient
change number names to "test.txt"
[m,n]=size(test); %Matrix dimensions
out=test(1:1:m-6,:); %Define output variable
% Set Boundary condition t=0 & Re=2000
% Set Initial condition  t=0 & V(boundary)=0
for i=1:1:m-6 % Condition for 1st Point
   if test(i,2)==44.450001 | test(i,2) == -44.0001 | ...
         test(i,3)==50.00000 | test(i,3)==-50.00000
      out(i,4)=1/42*(39*test(i,4)+8*test(i+1,4)-4*test(i+2,4)-4*test(i+3,4) ...
         +test(i+4,4)+4*test(i+5,4)-2*test(i+6,4)); % Smoothing Eq.
      out(i,5)=1/42*(39*test(i,5)+8*test(i+1,5)-4*test(i+2,5)-4*test(i+3,5) ...
         +test(i+4,5)+4*test(i+5,5)-2*test(i+6,5)); % Smoothing Eq.
      out(i,6)=1/42*(39*test(i,6)+8*test(i+1,6)-4*test(i+2,6)-4*test(i+3,6) ...
         +test(i+4,6)+4*test(i+5,6)-2*test(i+6,6)); % Smoothing Eq.


      out(i,7)=60/252*(-
257*test(i,4)+122*test(i+1,4)+185*test(i+2,4)+72*test(i+3,4) ...
         -77*test(i+4,4)-122*test(i+5,4)+77*test(i+6,4)); %Sloping Eq.
      out(i,8)=60/252*(-
257*test(i,5)+122*test(i+1,5)+185*test(i+2,5)+72*test(i+3,5) ...
         -77*test(i+4,5)-122*test(i+5,5)+77*test(i+6,5)); %Sloping Eq.
      out(i,9)=60/252*(-
257*test(i,6)+122*test(i+1,6)+185*test(i+2,6)+72*test(i+3,6) ...
         -77*test(i+4,6)-122*test(i+5,6)+77*test(i+6,6)); %Sloping Eq.

   elseif test(i,2)==40.005001 | test(i,2) == -40.005001 | ...
         test(i,3)==45.0000 | test(i,3)==-45.00000  % Condition for 2nd Point
      out(i+1,4)=1/42*(8*test(i,4)+19*test(i+1,4)+16*test(i+2,4)+6*test(i+3,4)
...
         -4*test(i+4,4)-7*test(i+5,4)+4*test(i+6,4)); % Smoothing Eq.
      out(i+1,5)=1/42*(8*test(i,5)+19*test(i+1,5)+16*test(i+2,5)+6*test(i+3,5)
...
         -4*test(i+4,5)-7*test(i+5,5)+4*test(i+6,5)); % Smoothing Eq.
      out(i+1,6)=1/42*(8*test(i,6)+19*test(i+1,6)+16*test(i+2,6)+6*test(i+3,6)
...
         -4*test(i+4,6)-7*test(i+5,6)+4*test(i+6,6)); % Smoothing Eq.

      out(i,7)=60/252*(-
122*test(i,4)+17*test(i+1,4)+62*test(i+2,4)+48*test(i+3,4) ...
          +10*test(i+4,4)-17*test(i+5,4)+2*test(i+6,4)); %Sloping Eq.
      out(i,8)=60/252*(-
122*test(i,5)+17*test(i+1,5)+62*test(i+2,5)+48*test(i+3,5) ...
          +10*test(i+4,5)-17*test(i+5,5)+2*test(i+6,5)); %Sloping Eq.
      out(i,9)=60/252*(-
122*test(i,6)+17*test(i+1,6)+62*test(i+2,6)+48*test(i+3,6) ...
         +10*test(i+4,6)-17*test(i+5,6)+2*test(i+6,6));  %Sloping Eq.

   elseif test(i,2)==35.560001 | test(i,2) == -35.560001 | ...
          test(i,3)==40.0000 | test(i,3)==-40.00000  % Condition for 3rd Point
      out(i+2,4)=1/42*(-
4*test(i,4)+16*test(i+1,4)+19*test(i+2,4)+12*test(i+3,4) ...
         +2*test(i+4,4)-4*test(i+5,4)+test(i+6,4)); % Smoothing Eq.
      out(i+2,5)=1/42*(-
4*test(i,5)+16*test(i+1,5)+19*test(i+2,5)+12*test(i+3,5) ...
         +2*test(i+4,5)-4*test(i+5,5)+test(i+6,5)); % Smoothing Eq.
```

```
      out(i+2,6)=1/42*(-
4*test(i,6)+16*test(i+1,6)+19*test(i+2,6)+12*test(i+3,6) ...
         +2*test(i+4,6)-4*test(i+5,6)+test(i+6,6)); % Smoothing Eq.

      out(i+2,7)=60/252*(-29*test(i,4)-46*test(i+1,4)-
19*test(i+2,4)+24*test(i+3,4) ...
          +55*test(i+4,4)+46*test(i+5,4)-31*test(i+6,4)); %Sloping Eq.
      out(i+2,8)=60/252*(-29*test(i,5)-46*test(i+1,5)-
19*test(i+2,5)+24*test(i+3,5) ...
          +55*test(i+4,5)+46*test(i+5,5)-31*test(i+6,5)); %Sloping Eq.
      out(i+2,9)=60/252*(-29*test(i,6)-46*test(i+1,6)-
19*test(i+2,6)+24*test(i+3,6) ...
          +55*test(i+4,6)+46*test(i+5,6)-31*test(i+6,6)); %Sloping Eq.

    else % For other points
      out(i+3,4)=1/21*(-2*test(i-3,4)+3*test(i-2,4)+6*test(i-1,4)+7*test(i,4)
...
         +6*test(i+1,4)+3*test(i+2,4)-2*test(i+3,4)); % Smoothing Eq.
      out(i+3,5)=1/21*(-2*test(i-3,5)+3*test(i-2,5)+6*test(i-1,5)+7*test(i,5)
...
         +6*test(i+1,5)+3*test(i+2,5)-2*test(i+3,5)); % Smoothing Eq.
      out(i+3,6)=1/21*(-2*test(i-3,6)+3*test(i-2,6)+6*test(i-1,6)+7*test(i,6)
...
         +6*test(i+1,6)+3*test(i+2,6)-2*test(i+3,6)); % Smoothing Eq.

      out(i+3,7)=60/252*(22*test(i-3,4)-67*test(i-2,4)-58*test(i-1,4)+ ...
         58*test(i+1,4)+67*test(i+2,4)-22*test(i+3,4)); %Sloping Eq.
      out(i+3,8)=60/252*(22*test(i-3,5)-67*test(i-2,5)-58*test(i-1,5)+ ...
         58*test(i+1,5)+67*test(i+2,5)-22*test(i+3,5)); %Sloping Eq.
      out(i+3,9)=60/252*(22*test(i-3,6)-67*test(i-2,6)-58*test(i-1,6)+ ...
         58*test(i+1,6)+67*test(i+2,6)-22*test(i+3,6)); %Sloping Eq.
   end
end
% The last three rows are the left points by using 3-degree, 7-point
polynomial.

last_three=test(m-11:1:m,:);
temp=test(m-11:1:m,:);
[mm,nn]=size(temp); %Matrix dimensions
for i=mm:-1:mm-3
   if temp(i,2)==44.450001 | temp(i,2) == -44.0001 | ...
         temp(i,3)==50.00000 | temp(i,3)==-50.00000
      las_three(i,4)=1/42*(-4*temp(i,4)+16*temp(i-1,4)+19*temp(i-
2,4)+12*temp(i-3,4) ...
         +2*temp(i-4,4)-4*temp(i-5,4)+temp(i-6,4)); % Smoothing Eq.
      las_three(i,5)=1/42*(-4*temp(i,5)+16*temp(i-1,5)+19*temp(i-
2,5)+12*temp(i-3,5) ...
         +2*temp(i-4,5)-4*temp(i-5,5)+temp(i-6,5)); % Smoothing Eq.
      las_three(i,6)=1/42*(-4*temp(i,6)+16*temp(i-1,6)+19*temp(i-
2,6)+12*temp(i-3,6) ...
         +2*temp(i-4,6)-4*temp(i-5,6)+temp(i-6,6)); % Smoothing Eq.

      las_three(i,7)=60/252*(-257*temp(i,4)+122*temp(i-1,4)+185*temp(i-
2,4)+72*temp(i-3,4) ...
         -77*temp(i-4,4)-122*temp(i-5,4)+77*temp(i-6,4)); %Sloping Eq.
      las_three(i,8)=60/252*(-257*temp(i,5)+122*temp(i-1,5)+185*temp(i-
2,5)+72*temp(i-3,5) ...
         -77*temp(i-4,5)-122*temp(i-5,5)+77*temp(i-6,5)); %Sloping Eq.
      las_three(i,9)=60/252*(-257*temp(i,6)+122*temp(i-1,6)+185*temp(i-
2,6)+72*temp(i-3,6) ...
         -77*temp(i-4,6)-122*temp(i-5,6)+77*temp(i-6,6)); %Sloping Eq.
   elseif temp(i,2)==40.005001 | temp(i,2) == -40.005001 | ...
```

```
         temp(i,3)==45.0000 | temp(i,3)==-45.00000
      las_three(i-1,4)=1/42*(8*temp(i,4)+19*temp(i-1,4)+16*temp(i-
2,4)+6*temp(i-3,4) ...
         -4*temp(i-4,4)-7*temp(i-5,4)+4*temp(i-6,4)); % Smoothing Eq.
      las_three(i-1,5)=1/42*(8*temp(i,5)+19*temp(i-1,5)+16*temp(i-
2,5)+6*temp(i-3,5) ...
         -4*temp(i-4,5)-7*temp(i-5,5)+4*temp(i-6,5)); % Smoothing Eq.
      las_three(i-1,6)=1/42*(8*temp(i,6)+19*temp(i-1,6)+16*temp(i-
2,6)+6*temp(i-3,6) ...
         -4*temp(i-4,6)-7*temp(i-5,6)+4*temp(i-6,6)); % Smoothing Eq.

      las_three(i,7)=60/252*(-122*temp(i,4)+17*temp(i-1,4)+62*temp(i-
2,4)+48*temp(i-3,4) ...
          +10*temp(i-4,4)-17*temp(i-5,4)+2*temp(i-6,4)); %Sloping Eq.
      las_three(i,8)=60/252*(-122*temp(i,5)+17*temp(i-1,5)+62*temp(i-
2,5)+48*temp(i-3,5) ...
          +10*temp(i-4,5)-17*temp(i-5,5)+2*temp(i-6,5)); %Sloping Eq.
      las_three(i,9)=60/252*(-122*temp(i,6)+17*temp(i-1,6)+62*temp(i-
2,6)+48*temp(i-3,6) ...
         +10*temp(i-4,6)-17*temp(i-5,6)+2*temp(i-6,6));  %Sloping Eq.

   else

      las_three(i-2,4)=1/42*(39*temp(i,4)+8*temp(i-1,4)-4*temp(i-2,4)-4*temp(i-
3,4) ...
         +temp(i-4,4)+4*temp(i-5,4)-2*temp(i-6,4)); % Smoothing Eq.
      las_three(i-2,5)=1/42*(39*temp(i,5)+8*temp(i-1,5)-4*temp(i-2,5)-4*temp(i-
3,5) ...
         +temp(i-4,5)+4*temp(i-5,5)-2*temp(i-6,5)); % Smoothing Eq.
      las_three(i-2,6)=1/42*(39*temp(i,6)+8*temp(i-1,6)-4*temp(i-2,6)-4*temp(i-
3,6) ...
         +temp(i-4,6)+4*temp(i-5,6)-2*temp(i-6,6)); % Smoothing Eq.

      las_three(i-2,7)=60/252*(22*temp(i,4)-67*temp(i-1,4)-58*temp(i-2,4) ...
          +58*temp(i-4,4)+67*temp(i-5,4)-22*temp(i-6,4)); %Sloping Eq.
      las_three(i-2,8)=60/252*(22*temp(i,5)-67*temp(i-1,5)-58*temp(i-2,5) ...
          +58*temp(i-4,5)+67*temp(i-5,5)-22*temp(i-6,5)); %Sloping Eq.
      las_three(i-2,9)=60/252*(22*temp(i,6)-67*temp(i-1,6)-58*temp(i-2,6) ...
         +58*temp(i-4,6)+67*temp(i-5,6)-22*temp(i-6,6));  %Sloping Eq.
   end
end

for i=1:1:m-6
   if out(i,4)==0
      out(i,10)=0;
   else
      out(i,10)=out(i,7)/out(i,4);
   end
   if out(i,5)==0
      out(i,11)=0;
   else
      out(i,11)=out(i,8)/out(i,5);
   end
   if out(i,6)==0
      out(i,12)=0;
   else
      out(i,12)=out(i,9)/out(i,6);
   end
   if out(i,6)==0
      out(i,13)=0;
   else
      out(i,13)=out(i,7)/out(i,6);
```

```
   end
   if out(i,6)==0
      out(i,14)=0;
   else
      out(i,14)=out(i,8)/out(i,6);
   end
   if out(i,6)==0
      out(i,15)=0;
   else
      out(i,15)=out(i,9)/out(i,6);
   end
   out(i,16) = -out(i,15)-out(i,11);


end

for i=6:-1:1
   if last_three(i,4)==0
      last_three(i,10)=0;
   else
      last_three(i,10)=last_three(i,7)/last_three(i,5);
   end
   if last_three(i,5)==0
      last_three(i,11)=0;
   else
      last_three(i,11)=last_three(i,8)/last_three(i,5);
   end
   if last_three(i,5)==0
      last_three(i,12)=0;
   else
      last_three(i,12)=last_three(i,9)/last_three(i,5);
   end

   if last_three(i,6)==0
      last_three(i,13)=0;
   else
      last_three(i,13)=last_three(i,7)/last_three(i,6);
   end
   if last_three(i,6)==0
      last_three(i,14)=0;
   else
      last_three(i,14)=last_three(i,8)/last_three(i,6);
   end
   if last_three(i,6)==0
      last_three(i,15)=0;
   else
      last_three(i,15)=last_three(i,9)/last_three(i,6);
   end
   last_three(i,16) = -last_three(i,15)-last_three(i,11);

end

out=[out
   last_three]; % Combine the last three rows with other rows.
kk=0; % This loop is a note to tell every 1-441
for i=1:441:m
   kk=kk+1;
   for j=i:1:(i+441)
      out(j,17)=kk;
   end

end
```

```
 save out.dat out -ascii %Save File as out.dat
% At last, we need to delete three rows which are from last 6 to last 12 rows,
and combine the left together.
% The output result consists of 19 columns: first three columns are X,Y,Z
position; Second three columns are smoothing Ux,Uy,Uz velocities;
% Third three columns are sloping; Next six columns are the six derivitives;
the last one Ux/x is we need to compare.
```

```
%   TH.m  for calculation by using continuity equation and Taylor's hypothesis.
%   This program calculates the velocity directive by using Taylor's hypothesis
and continuity equation.
%   Dong Zhang 11/15/2001
%   test_1.dat file has the overall velocities and local velocities.
load t1.dat; %Load 11-point average grid files, change number names to
"t1...7.dat"
load t2.dat;load t3.dat;load t4.dat;load t5.dat;load t6.dat;load t7.dat;
load test_1.dat
[m,n]=size(t1); % Matrix dimensions
test=t1;
out=test(1:1:m,:); %Define output variable
% Set Boundary condition t=0 & Re=2000
% Set Initial condition  t=0 & V(boundary)=0
for i=1:1:m% Condition for 1st Point
   if t1(i,2)==44.450001 | t1(i,2) == -44.0001 | ...
         t1(i,3)==50.00000 | t1(i,3)==-50.00000
      out(i,4)=1/42*(39*t1(i,4)+8*t2(i,4)-4*t3(i,4)-4*t4(i,4) ...
         +t5(i,4)+4*t6(i,4)-2*t7(i,4)); % Smoothing Eq.
      out(i,5)=1/42*(39*t1(i,5)+8*t2(i,5)-4*t3(i,5)-4*t4(i,5) ...
         +t5(i,5)+4*t6(i,5)-2*t7(i,5)); % Smoothing Eq.
      out(i,6)=1/42*(39*t1(i,6)+8*t2(i,6)-4*t3(i,6)-4*t4(i,6) ...
         +t5(i,6)+4*t6(i,6)-2*t7(i,6)); % Smoothing Eq.


      out(i,7)=60/252*(-257*t1(i,4)+122*t2(i,4)+185*t3(i,4)+72*t4(i,4) ...
         -77*t5(i,4)-122*t6(i,4)+77*t7(i,4)); %Sloping Eq.
      out(i,8)=60/252*(-257*t1(i,5)+122*t2(i,5)+185*t3(i,5)+72*t4(i,5) ...
         -77*t5(i,5)-122*t6(i,5)+77*t7(i,5)); %Sloping Eq.
      out(i,9)=60/252*(-257*t1(i,6)+122*t2(i,6)+185*t3(i,6)+72*t4(i,6) ...
         -77*t5(i,6)-122*t6(i,6)+77*t7(i,6)); %Sloping Eq.

   elseif t1(i,2)==40.005001 | t1(i,2) == -40.005001 | ...
         t1(i,3)==45.0000 | t1(i,3)==-45.00000  % Condition for 2nd Point
      out(i+1,4)=1/42*(8*t1(i,4)+19*t2(i,4)+16*t3(i,4)+6*t4(i,4) ...
         -4*t5(i,4)-7*t6(i,4)+4*t7(i,4)); % Smoothing Eq.
      out(i+1,5)=1/42*(8*t1(i,5)+19*t2(i,5)+16*t3(i,5)+6*t4(i,5) ...
         -4*t5(i,5)-7*t6(i,5)+4*t7(i,5)); % Smoothing Eq.
      out(i+1,6)=1/42*(8*t1(i,6)+19*t2(i,6)+16*t3(i,6)+6*t4(i,6) ...
         -4*t5(i,6)-7*t6(i,6)+4*t7(i,6)); % Smoothing Eq.

      out(i,7)=15/252*(-122*t1(i,4)+17*t2(i,4)+62*t3(i,4)+48*t4(i,4) ...
          +10*t5(i,4)-17*t6(i,4)+2*t7(i,4)); %Sloping Eq.
      out(i,8)=15/252*(-122*t1(i,5)+17*t2(i,5)+62*t3(i,5)+48*t4(i,5) ...
          +10*t5(i,5)-17*t6(i,5)+2*t7(i,5)); %Sloping Eq.
      out(i,9)=15/252*(-122*t1(i,6)+17*t2(i,6)+62*t3(i,6)+48*t4(i,6) ...
         +10*t5(i,6)-17*t6(i,6)+2*t7(i,6));  %Sloping Eq.

   elseif t1(i,2)==35.560001 | t1(i,2) == -35.560001 | ...
          t1(i,3)==40.0000 | t1(i,3)==-40.00000  % Condition for 3rd Point
      out(i+2,4)=1/42*(-4*t1(i,4)+16*t2(i,4)+19*t3(i,4)+12*t4(i,4) ...
         +2*t5(i,4)-4*t6(i,4)+t7(i,4)); % Smoothing Eq.
      out(i+2,5)=1/42*(-4*t1(i,5)+16*t2(i,5)+19*t3(i,5)+12*t4(i,5) ...
         +2*t5(i,5)-4*t6(i,5)+t7(i,5)); % Smoothing Eq.
      out(i+2,6)=1/42*(-4*t1(i,6)+16*t2(i,6)+19*t3(i,6)+12*t4(i,6) ...
         +2*t5(i,6)-4*t6(i,6)+t7(i,6)); % Smoothing Eq.

      out(i+2,7)=15/252*(-29*t1(i,4)-46*t2(i,4)-19*t3(i,4)+24*t4(i,4) ...
          +55*t5(i,4)+46*t6(i,4)-31*t7(i,4)); %Sloping Eq.
      out(i+2,8)=15/252*(-29*t1(i,5)-46*t2(i,5)-19*t3(i,5)+24*t4(i,5) ...
          +55*t5(i,5)+46*t6(i,5)-31*t7(i,5)); %Sloping Eq.
      out(i+2,9)=15/252*(-29*t1(i,6)-46*t2(i,6)-19*t3(i,6)+24*t4(i,6) ...
```

```
          +55*t5(i,6)+46*t6(i,6)-31*t7(i,6)); %Sloping Eq.

    else % For other points
      out(i+3,4)=1/21*(-2*test(i-3,4)+3*test(i-2,4)+6*test(i-1,4)+7*t1(i,4) ...
         +6*t2(i,4)+3*t3(i,4)-2*t4(i,4)); % Smoothing Eq.
      out(i+3,5)=1/21*(-2*test(i-3,5)+3*test(i-2,5)+6*test(i-1,5)+7*t1(i,5) ...
         +6*t2(i,5)+3*t3(i,5)-2*t4(i,5)); % Smoothing Eq.
      out(i+3,6)=1/21*(-2*test(i-3,6)+3*test(i-2,6)+6*test(i-1,6)+7*t1(i,6) ...
         +6*t2(i,6)+3*t3(i,6)-2*t4(i,6)); % Smoothing Eq.

      out(i+3,7)=15/252*(22*test(i-3,4)-67*test(i-2,4)-58*test(i-1,4)+ ...
         58*t2(i,4)+67*t3(i,4)-22*t4(i,4)); %Sloping Eq.
      out(i+3,8)=15/252*(22*test(i-3,5)-67*test(i-2,5)-58*test(i-1,5)+ ...
         58*t2(i,5)+67*t3(i,5)-22*t4(i,5)); %Sloping Eq.
      out(i+3,9)=15/252*(22*test(i-3,6)-67*test(i-2,6)-58*test(i-1,6)+ ...
         58*t2(i,6)+67*t3(i,6)-22*t4(i,6)); %Sloping Eq.
   end
end
% The last three rows are the left points by using 3-degree, 7-point
polynomial.
out(:,10)=test_1;
for i=1:1:m
   if out(i,7)==0
      out(i,11)=0;
   else
      out(i,11)=out(i,7)/out(i,7);
   end
   if out(i,7)==0
      out(i,12)=0;
   else
      out(i,12)=out(i,8)/out(i,7);
   end
   if out(i,7)==0
      out(i,13)=0;
   else
      out(i,13)=out(i,9)/out(i,7);
   end
end

out2=out;
save out2.dat out2 -ascii %Save File as out2.dat
% At last, we need to delete three rows which are from last 6 to last 12 rows,
and combine the left together.
% The output result consists of 10 columns: First three columns are smoothing
Ux, Uy, Uz velocities; second three columns are sloping;
% Third seventh column is the average velocity at every point; Next three
columns are the three derivatives; the eighth one is we need to compare.
```